Journal of Nanobiotechnology

RESEARCH

Open Access

Preferential activation of type I interferon-mediated antitumor inflammatory signaling by CuS/MnO_2/diAMP nanoparticles enhances anti-PD-1 therapy for sporadic colorectal cancer

Jinrong Peng[1*], Qian Yang[2*], Rong Lei[2], Yue Wang[2], Gansha Liu[2] and Zhiyong Qian[1*]

Abstract

Converting the "cold" tumor microenvironment (TME) to a "hot" milieu has become the prevailing approach for enhancing the response of immune-excluded/immunosuppressed colorectal cancer (CRC) patients to immune checkpoint blockade (ICB) therapy. During this process, inflammation accompanied by different kinds of chemokines/cytokines inevitably occurs. However, some activated inflammatory signals exhibit protumor potency. Therefore, strategies that preferentially activate antitumor inflammatory signaling rather than tumor-promoting signaling need to be developed. Herein, we constructed a STING agonist-loaded CuS/MnO_2 bimetallic nanosystem, termed diAMP-BCM. BCM with an optimized Cu/Mn ratio efficiently promoted the activation of proinflammatory signaling, and in combination with the STING agonist diAMP, diAMP-BCM controllably activated tumoricidal inflammatory signaling in APCs. DiAMP-BCM can efficiently generate ROS and promote the activation of STING, which induces the apoptosis of cancer cells and promotes the recruitment of monocytes while facilitating the polarization of macrophages and maturation of DCs. MC38 and CT26 CRC models were established to evaluate the in vivo antitumor effects of diAMP-BCM. Combined with ICB therapy, diAMP-BCM enables the rebuilding of tumor milieus with efficient tumor growth inhibition and alleviation of T-cell exhaustion, particularly in distal tumors, in sporadic colorectal cancer therapy. This study established a nanoplatform to promote the preferential activation of antitumor inflamatory signaling, rebuild the T-cell repertoire and alleviate T-cell exhaustion to enhance cancer ICB immunotherapy.

Highlights

1. DiAMP-BCM hybrid nanoparticles preferentially activate antitumor inflammatory signaling via STING/IRF7/CXCL10 axis and alleviate the expressions of protumor cytokines.

*Correspondence:
Jinrong Peng
rater.peng@163.com
Qian Yang
yoyoyoung@cmc.edu.cn
Zhiyong Qian
anderson-qian@163.com

2. DiAMP-BCM induces apoptosis/pyroptosis of colorectal cancer cells, promotes the recruitment of monocytes and their differentiation to pro-inflammatory phenotypes.
3. DiAMP-BCM converts an immunosuppressive tumor to a "hot" tumor and alleviates T cell exhaustion in vivo, which enhances the efficacy of aPD-1 immunotherapy in vivo and promotes the inhibition of both primary and distant colorectal tumors.

Introduction

Colorectal cancer (CRC) is a malignant cancer with high mortality and risk, and the number of new cases is increasing annually [1]. At the time of diagnosis, more than 50% of CRC patients are at stage III or IV, and surgery cannot be performed for these patients. Moreover, sporadic features and immune exclusion characteristics further limit the therapeutic outcome of CRC patients treated with radiotherapy and chemotherapy. Immune checkpoint blockade (ICB) provides another option for CRC therapy by invigorating the immune system [2]. The response rate of dMMR/MSI-H CRC patients (~ 15% of total CRC patients) to ICB has been reported to be approximately 90%, and patients with the pMMR/MSS CRC phenotype still exhibit a low or even no response to ICB [3, 4]. Moreover, more than 30% of dMMR CRC patients suffer primary or acquired resistance to ICB [5]. The construction of efficient strategies that enhance the response of pan-CRC to ICB remains a challenge.

The main reason for the low/no response of pMMR/MSS CRC to ICB may be the "cold" tumor microenvironment (TiME), which features low infiltration of immunocytes and immunosuppressive milieus [6]. Some of the strategies focusing on turning "cold" TiME to "hot" TiME have proven the potential of TiME "reinflaming" for enhancing the efficacy of CRC ICB therapy. However, turning a "cold" tumor to a "hot" tumor also aggravates intratumoral inflammation. High inflammation (high expression of IL-6 serving as the main indicator) is strongly correlated with poor survival outcomes among stage III CRC patients [7]. It can promote the progression of CRC and is also responsible for the formation of an immunosuppressive tumor immune microenvironment (TiME). Furthermore, inflammation is also responsible for the acquisition of resistance to ICB in dMMR-MSI-H CRC [8]. Conversely, the pleiotropic and complex inherence of inflammation to versatile related chemokines and cytokines makes it crucial for the reinforcement of antitumor immunity [9, 10]. Preferential activation of specific inflammatory signaling pathways can be achieved by adjusting the network and constitution of cytokines and chemokines, e.g., the NF-kB/IL6/STAT3 axis mediates the inflammatory response to promote cancer progression, while the type I interferon response favors the stimulation of antitumor immunity [9, 11–13]. Therefore, to efficiently enhance the response of CRC to ICB, strategies promoting the activation of antitumor proinflammatory signaling, rather than tumor-promoting signaling, need to be developed [14].

Metal-based nanosystems are promising due to their versatile catalytic performance in various cellular environments [15]. As a previous report indicated, CuxS nanosystems can generate ROS after $Cu2^+$ is released into the redox environment and reacts with GSH or H_2O_2 [16–19]. CuxS also has the potential to react with H_2O_2 to generate O_2 [20]. Moreover, in the presence of H_2O_2, manganese dioxide (MnO_2) can serve as an O_2 generator [21]; nonetheless, in the presence of GSH, MnO_2 preferentially reacts with GSH to produce $Mn2^+$ and oxidize GSH to GSSG [22]. Then, the released Mn^{2+} will further react with H_2O_2 to generate ROS. The products of metal-based nanosystems are mainly dependent on the surrounding environment, which including the pH value, oxygen levels, and radical levels, etc. Furthermore, Mn^{2+} also stimulates STING [23, 24], which is the main signaling pathway that promotes the generation of a type I interferon response in cells; however, Mn^{2+} also promotes the activation of the NK-kB pathway to promote the production of TNFa, IL-6, IL-1b, etc. [25, 26]. In addition, STING can be activated by externally supplied cyclic diadenosine monophosphate (diAMP), and Mn^{2+} has the potential to further enhance cyclic diadenosine monophosphate (diAMP)-mediated STING activation [27, 28]. However, activation of STING alone cannot direct or promote inflammatory signaling through antitumor immunity. In addition, it has been demonstrated that the type I interferon response induced by STING requires STING to be translocated from the endoplasmic reticulum (ER) to late endosomes or that autophagy can be inhibited [29–31]. Decreased production of intracellular ROS or increased generation of intracellular oxygen in APCs facilitates the inhibition of autophagy, thus promoting the translocation of STING from the ER to late endosomes. The potential of MnO_2 to alleviate hypoxia in vitro and in vivo has been verified, as has its ability to activate STING. However, the introduction of CuS and diAMP is also required to enhance ROS production to inhibit the growth of tumor cells and to supply DNA

segments for the efficient activation of STING. Hence, due to the different properties of CuS and MnO_2 in regulating cellular milieus, the combination of CuS and MnO_2 may provide an option for preferentially activating antitumor inflammatory signaling.

Therefore, in this study, we first prepared CuS (BC) and MnO_2 (BM) nanoparticles via nanoprecipitation/nanomineralization with bovine serum albumin (BSA), respectively. After comprehensively evaluating their catalytic properties and cellular activities in vitro, we further evaluated the effect of the combination of BC and BM on APC behavior by optimizing the ratios. Then, we constructed BCM nanoparticles via a two-step procedure and adsorbed a STING agonist (diAMP) to obtain diAMP-BCM nanohybrids. The effects of the diAMP-BCM nanohybrid on the cytotoxicity of tumor cells and the regulation of the cellular behavior of APCs were also studied in detail. More importantly, the potential of diAMP-BCM to remodel the TiME, particularly when combined with aPD-1, was also evaluated. Two different CRC tumor models, MC38 and CT26, were established. The in vitro and in vivo results demonstrated that optimized diAMP-BCM can controllably activate antitumor immune inflammatory signaling, enhance the therapeutic effects of ICB and alleviate T-cell exhaustion to inhibit both primary and distal sporadic tumor foci (Fig. 1).

Results

Preparation and characterization of BC and BM nanoparticles

According to our previous study [32, 33], we constructed BC and BM nanoparticles via nanoprecipitation in an aqueous environment in the presence of BSA. Well-dispersed BC and BM nanoparticles with uniform morphology were obtained (Fig. 2A). The particle sizes of the BC and BM nanoparticles were 8.4 ± 2.1 and 9.0 ± 3.4 nm, respectively, while the zeta potentials were ~ − 11 mV and ~ − 5 mV, respectively (Fig. 2B, C). The XRD patterns of BC and BM indicate the presence of CuS and MnO_2, although the presence of BSA decreased the number of

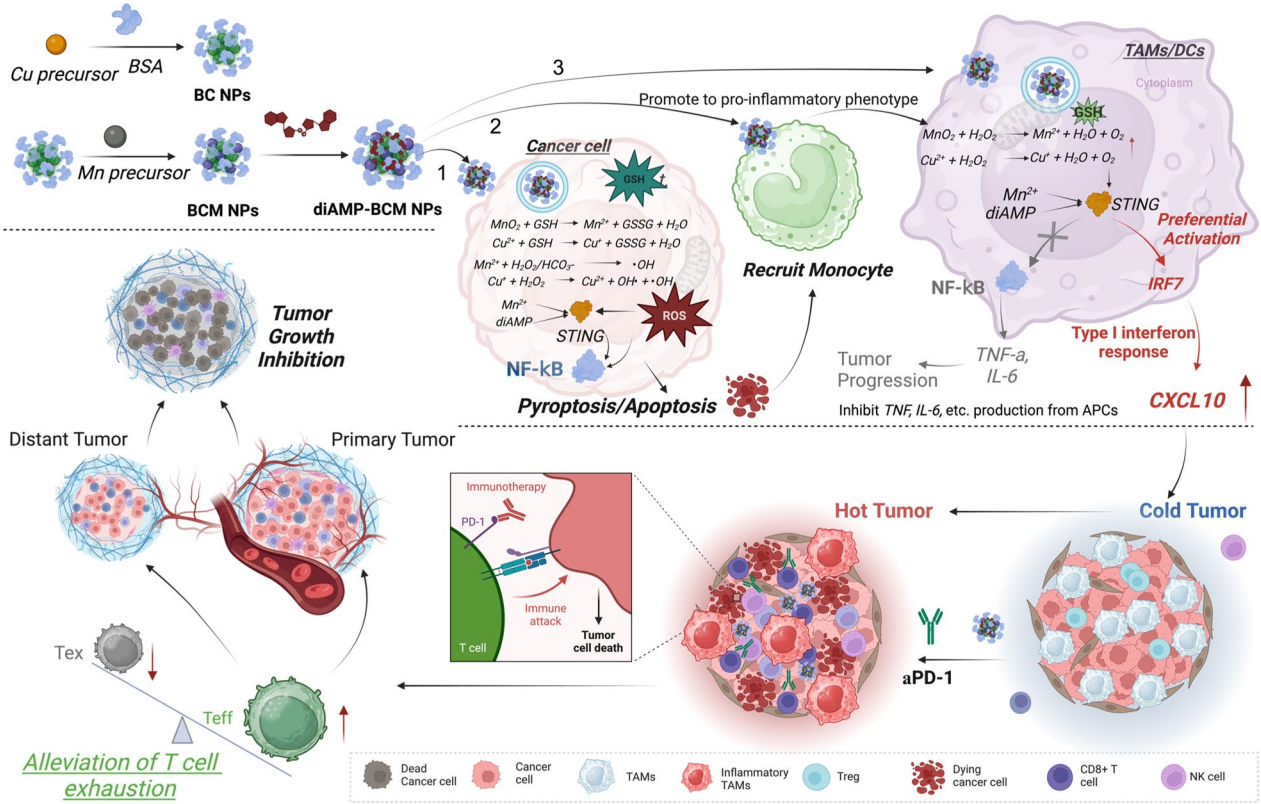

Fig. 1 Schematic showing that diAMP-BCM nanohybrids with optimized Cu/Mn ratios preferentially activate antitumor inflammatory signaling in APCs while promoting apoptosis in tumor cells. Tumor cells and APCs (macrophages and DCs) exhibit different intracellular physiological environments, which provide different environments for the intracellular reaction of metal-based nanoparticles, thus regulating inflammatory signaling. Here, the combination of BC and BM nanoparticles at optimized ratios promoted the generation of a type I interferon response, which was the result of antitumor inflammatory signaling, rather than NF-kB signaling, in combination with a STING agonist. The activation of the type I interferon response further reverses the "cold" TME to a "hot" milieu and further remodels the TME to alleviate T-cell exhaustion when combined with ICB therapy, which allows efficient management of both primary (treated) tumors and distal tumors

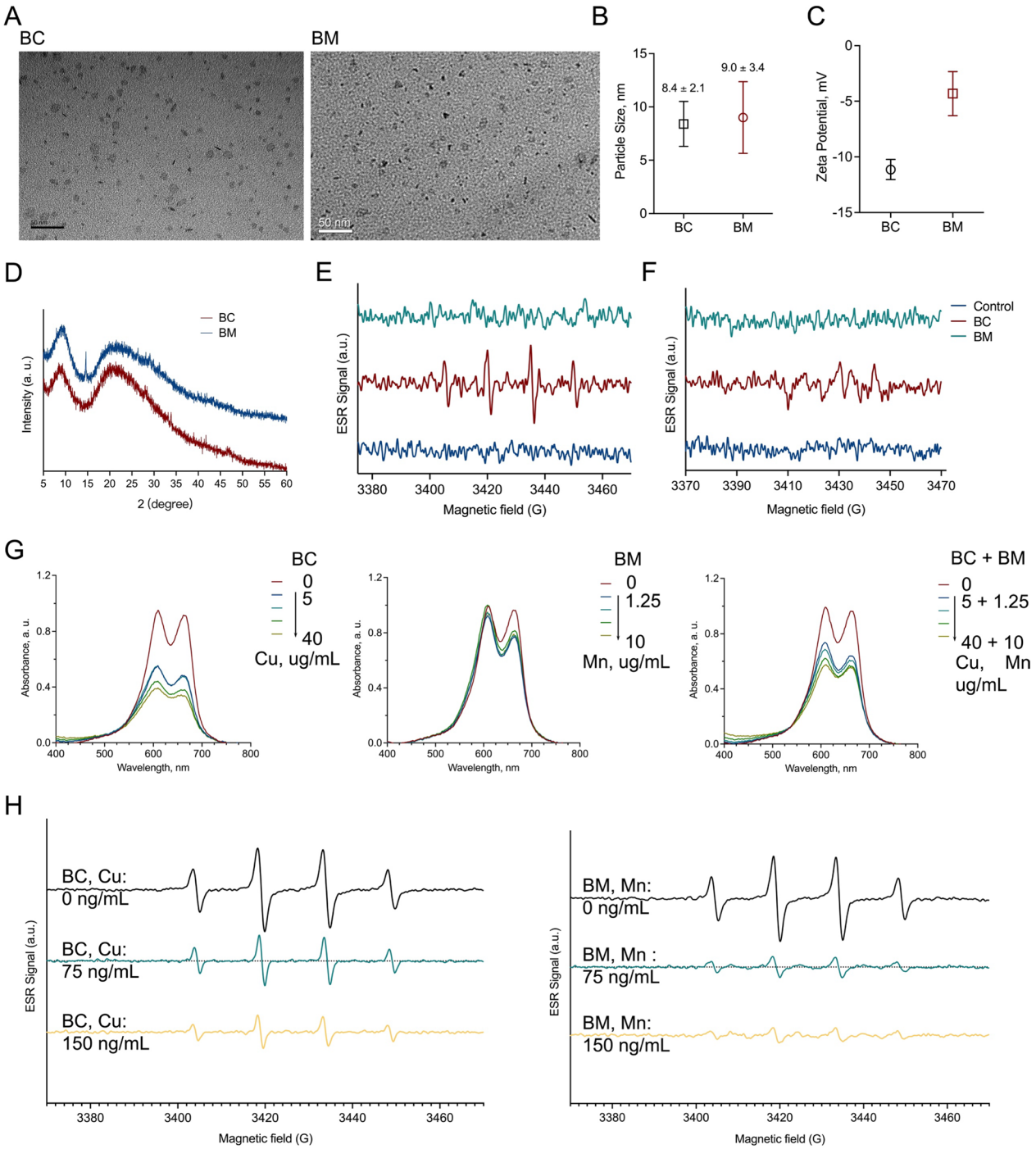

Fig. 2 Construction and characterization of BC and BM nanoparticles. **A** TEM images of BC and BM nanoparticles. **B** The particle sizes calculated from the TEM images. **C** The zeta potentials of the nanoparticles. **D** XRD patterns of BC and BM. **E** ESR spectra of.OH after the introduction of BC and BM, respectively, in a ·OH generation model assay. **F** ESR spectra of $\cdot O_2$ after the introduction of BC or BM. **G** UV–visible spectra of MB solutions after the introduction of BC, BM or a mixture of BC/BM at the same concentrations. **H** ESR spectra of ·OH after the introduction of BC and BM, respectively, in a ·OH deletion model assay

crystalline peaks (Fig. 2D). Then, we evaluated the catalytic performance of BCM in ROS generation and scavenging in vitro. Metal ions have been proven to exhibit catalytic activity similar to that of some enzymes in the Fenton reaction. Due to the universality of the imbalanced redox environment in solid tumors and the

overproduction of H_2O_2 in tumors, we evaluated the ability of BC and BM nanoparticles to catalyze the production of ROS in the presence of H_2O_2. BC nanoparticles and BM nanoparticles exhibited different performances in catalyzing the production of ROS. No enhanced electron spin resonance (ESR) signal was detected in the presence of BM nanoparticles in the DMPO/H_2O_2 solution, while the addition of BC nanoparticles enhanced the ESR signal of both. OH and $\cdot O_2$. This finding indicated that BC nanoparticles promote the generation of ROS, while BM nanoparticles do not (Fig. 2E, F). The ESR assay results are consistent with the ROS generation spectrometry results in an aqueous environment in the presence of MB (Fig. 3G). In contrast, in the case of ROS scavenging, the ESR signal of .OH significantly decreased after the addition of a low concentration of BM nanoparticles, while the signal intensity was similar to that of the blank sample. Although the addition of BC nanoparticles also decreased the ESR signal of .OH, the amplitude was much smaller than that of the BM nanoparticles (Fig. 3H). This finding demonstrated that BM nanoparticles facilitate the scavenging of ROS rather than promote the generation of ROS. BC and BM nanoparticles with different catalytic performances were successfully prepared. Created in BioRender. Peng, J.(2024) https://BioRender.com/f14i369.

Cellular activities of BC and BM nanoparticles in tumor cells and macrophages

Furthermore, the ability of BC and BM nanoparticles to induce ROS generation was also evaluated in vitro in the MC38 cell line and RAW264.7 macrophage line. The ROS signal was greater in the group cocultured with BC nanoparticles than in the BM nanoparticle-treated group, and the ROS generation in the BM nanoparticle-treated group was also significantly greater than that in the control group (Fig. 3A, B). This finding demonstrated that not only is the potential of BC nanoparticles to stimulate ROS generation maintained at the cellular level but also that BM nanoparticles can stimulate the generation of ROS. By measuring the mitochondrial membrane potential induced by JC-1, we further confirmed that both BC and BM nanoparticles decreased the mitochondrial membrane potential (increased green fluorescence intensity and decreased the red/green fluorescence ratio) (Fig. 3C), indicating the induction of ROS production from mitochondria (Fig. 3D).

Then, we further performed similar assays in vitro in the RAW264.7 macrophage line. With increasing BC nanoparticle concentrations, an increase in ROS generation was observed (Fig. 3E). In contrast, with the introduction of BM nanoparticles, the ROS generation of macrophages decreased at low concentrations of BM nanoparticles. As the concentration of BM nanoparticles increased, ROS generation increased slightly compared with that in the control group (Fig. 3E, F). Further evaluation of JC-1 staining in the RAW264.7 cell line revealed that the intensity of JC-1 monomers in BC-treated RAW264.7 cells increased, indicating the induction of ROS production from mitochondria, similar to the results in tumor cells. However, an increase in the intensity of JC-1 aggregates in BM-treated RAW264.7 cells was observed (Fig. 3G), which demonstrated that the BM nanoparticles did not promote ROS production from mitochondria and tended to strengthen mitochondrial integrity. Moreover, multiple pseudopod morphologies were observed in the BM-treated RAW264.7 cells, which indicated that the BM promoted RAW264.7 cell differentiation to the M1 phenotype, while the group treated with BC nanoparticles exhibited a morphology consistent with the M2 phenotype, and the number of pseudopods in the group treated with BM is significantly more than that treated with BC nanoparticles (Fig. 3H and Supplementary Fig. 1). Although ROS are the main promoters involved in the development of inflammatory signaling, different downstream signaling pathways control the direction of inflammatory signaling. The results indicate that the BM-treated RAW264.7 cells differentiated into proinflammatory cells via a signaling pathway different from that in the BC-treated group.

BC/BM combinations with different ratios activate different inflammatory signaling pathways

We further evaluated the effect of the combination of BC/BM nanoparticles at different ratios on the differentiation of macrophages [bone marrow-derived macrophages (BMDMs)]. The F4/80+CD86+ phenotype indicated the proinflammatory subtype. As the amount of BM increased (while the dose of BC increased), the proportion of F4/80+CD86+ BMDMs increased and reached a plateau, while the proportion of F4/80+CD86+ BMDMs peaked as the amount of BC increased (while the dose of BM decreased) (Fig. 3I, J). By further measuring the expression of genes related to inflammation in BMDMs after different treatments, we found that the expression levels of *CXCL10* and *IFNb*, which are indicators of the type I interferon response, were significantly increased in the group treated with BC/BM combined with Cu/Mn=4:1. Moreover, the expression levels of IL-6 and TNF, which are indicators of NK-kB-induced inflammation, were surprisingly decreased in this group (Fig. 3K). This indicates that the combination of BC/BM nanoparticles can regulate the differentiation of macrophages by optimizing the ratios of BC and BM.

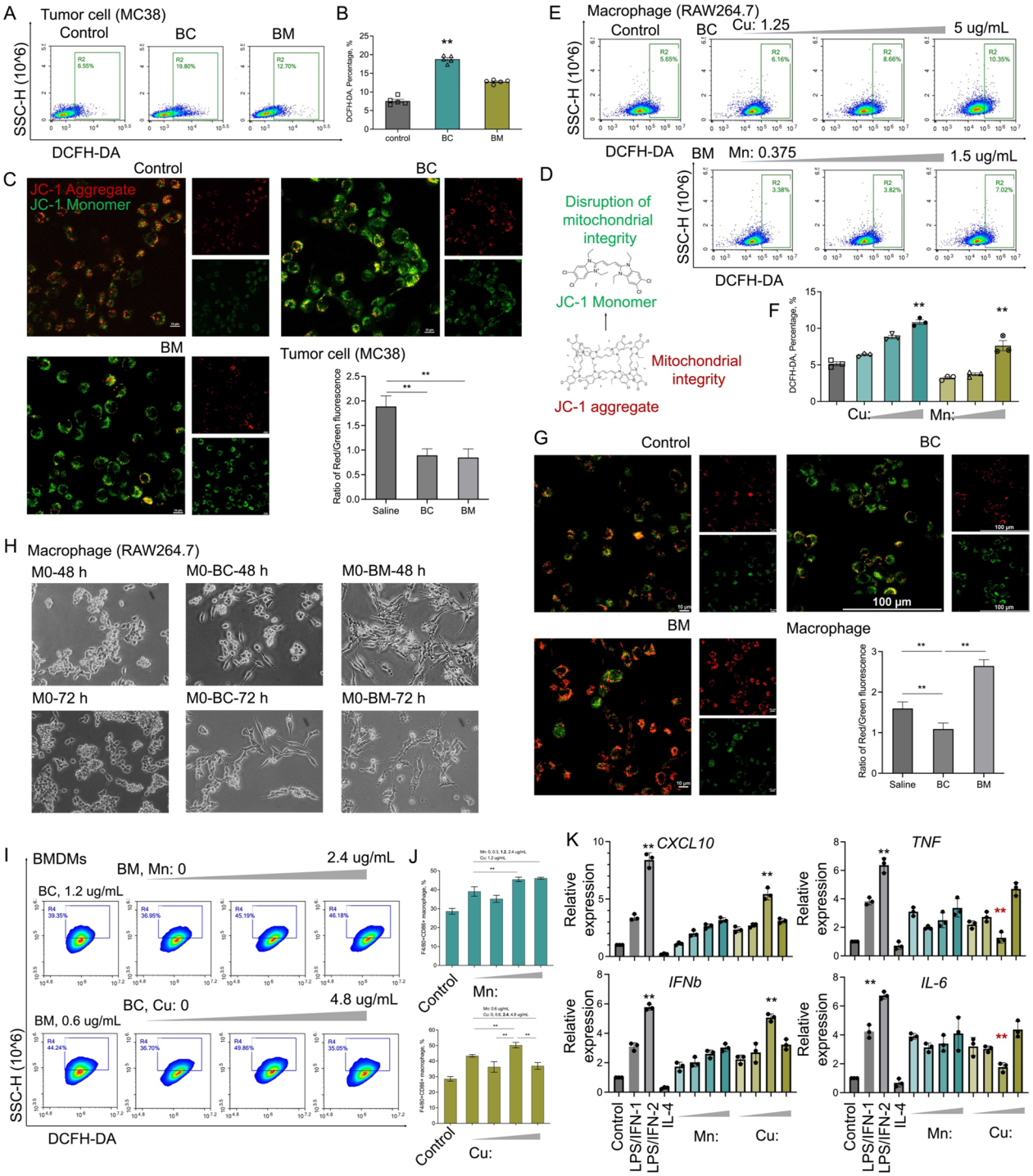

Fig. 3 **A**, **B** DCFH-DA-positive MC38 cells treated with BC and BM, respectively. **C** JC-1 fluorescence images of MC38 cells after treatment with BC or BM. **D** The mechanism by which JC-1 fluorescence changes. **E**, **F** DCFH-DA-positive RAW264.7 cells treated with BC and BM, respectively. **G** JC-1 fluorescence images of RAW264.7 cells after treatment with BC or BM. **H** DCM images of RAW264.7 cells after treatment with BC or BM. **I** Flow cytometry results of BMDMs treated with different combinations of BC/BM at different Cu/Mn ratios. **J** The proportions of F4/80+CD86+ cells in **I**. **K** Gene expression in the cell samples collected in **I**

Construction and characterization of BCM hybrid nanoparticles and diAMP-loaded BCM (diAMP-BCM) nanoparticles

Based on the above results, we further synthesized BCM nanoparticles via a two-step procedure: first, BSA-CuS (BC) nanoparticles were constructed, and then MnO_2 was precipitated from the BC nanoparticles (Fig. 4A). BCM nanoparticles with an average diameter of 25.3 ± 5.7 nm (observed by TEM, ~50 nm was measured by DLS) were obtained (Fig. 4B, C). The zeta potential of BCM was ~−7 mV. The XPS and XRD results further supported the successful linkage of Cu_xS and MnO_2 in the nanoparticles (Supplementary Figs. 2–4). Compared with BC and BM nanoparticles, BCM nanoparticles exhibit a core–shell morphology (low contraction in the core region and high contraction in the outer region)

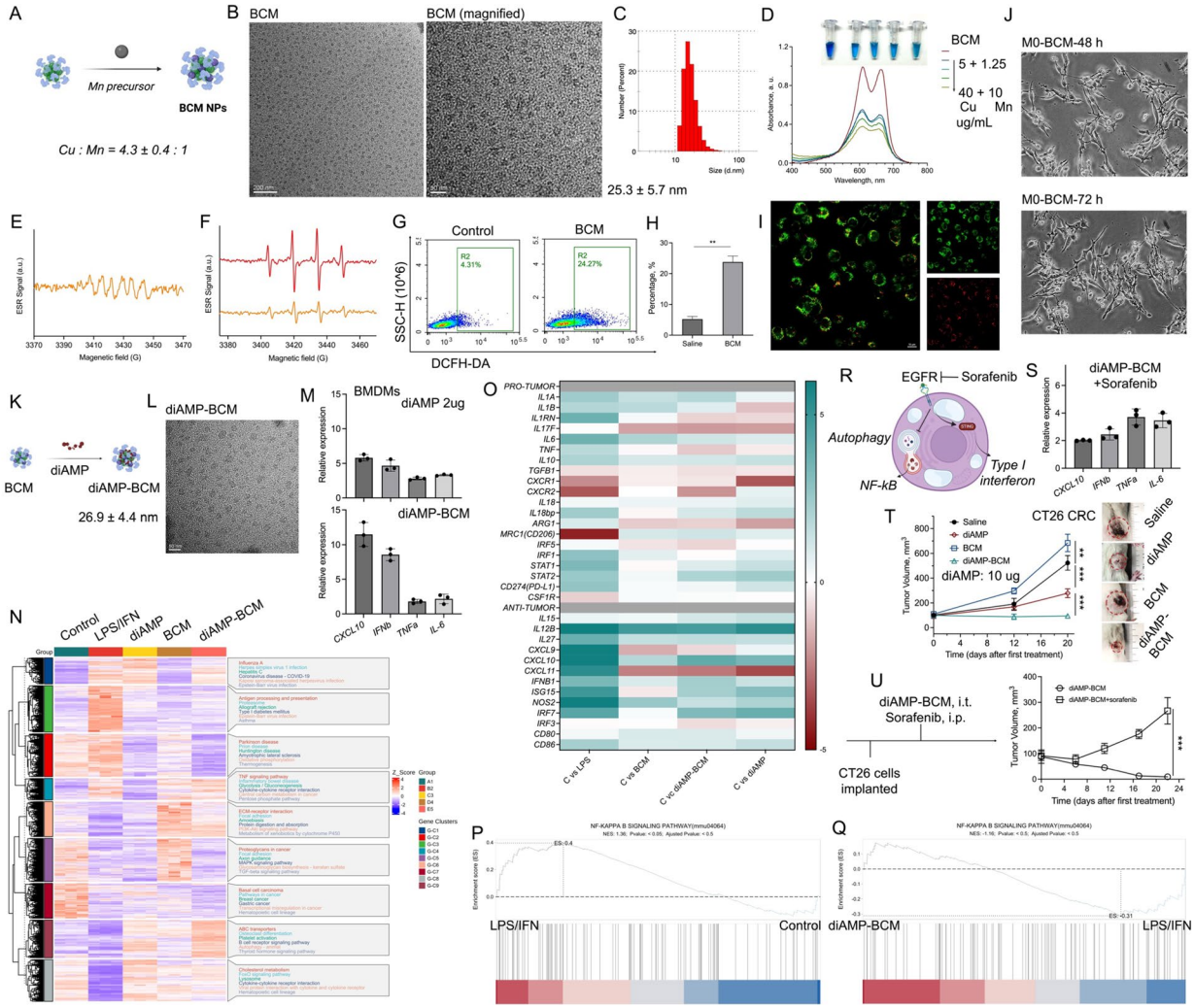

Fig. 4 **A** Preparation of BCM nanoparticles. **B** TEM images of BCM nanoparticles. **C** The particle size distribution of the BCM nanoparticles. **D** UV–visible spectra of MB solutions after the introduction of BCM. **E** ESR spectra of O_2 after the introduction of BCM. **F** ESR spectra of.OH after the introduction of BCM at different concentrations. **G**, **H** The generation of ROS in MC38 cells after the introduction of BCM nanoparticles. **I** Fluorescence images of MC38 cells treated with BCM and stained with JC-1. **J** DCM image of BMDMs after treatment with BCM. **K** Preparation of diAMP-BCM and **L** TEM image of diAMP-BCM. **M** The expression of inflammation-related genes in BMDMs after coculture with diAMP or diAMP-BCM. **N** Heatmap of gene expression in BMDMs after coculture with different samples, as measured by transcriptome sequencing, and the main pathways analyzed by KEGG are also listed. **O** Heatmap of the expression of the main genes related to inflammation, including protumor and antitumor genes. **P**, **Q** Enrichment of genes related to the NF-kB pathway after different treatments. **R** Illustration of the effect of EGFR on the activation of type I interferon. **S** The expression of inflammation-related genes in BMDMs after coculture with diAMP-BCM combined with the EGFR inhibitor sorafenib. **T**, **U** The in vivo inhibition of CT26 CRC by diAMP-BCM with or without the introduction of sorafenib, respectively

(Fig. 4B, enlargement). According to the ICP-AAS measurements, the contents of Cu and Mn in the BCM nanoparticles were 4.2 ± 0.4 μg/mg and 18.1 ± 3.2 μg/mg, respectively, with a Cu/Mn ratio of approximately 4.3:1. The UV–visible spectrum of the MB solution in the presence of H_2O_2 decreased dramatically after the addition of BCM nanoparticles, indicating the generation of ROS (Fig. 4D). Then, we evaluated the catalytic performance of BCM in vitro. Enhanced electron spin resonance (ESR) signals for both ·OH and $\cdot O_2$ were detected in the DMPO/H_2O_2 solution with the addition of BCM nanoparticles (Fig. 4E, F).

In cellular assays, the introduction of BCM nanoparticles promoted the generation of ROS in MC38 cells and triggered the dissociation of JC-1 aggregates and the release of JC-1 monomers (Fig. 4G–I). In addition, the coculturing of BCM nanoparticles and RAW264.7 cells promoted macrophage differentiation to an M1-like phenotype (Fig. 4J). The results demonstrated that the obtained BCM nanoparticles maintained the properties of the BC and BM nanoparticles.

DiAMP-BCM preferentially reinforces antitumor inflammatory signaling via the STING/IRF7/CXCL10 pathway

As BM nanoparticles exhibit different effects on tumor cells and macrophages and because Mn ion release from BM nanoparticles has the potential to stimulate STING, which can trigger the generation of a type I interferon response, we further adsorbed the STING agonist cyclic diadenosine monophosphate (diAMP) into BCM nanoparticles and obtained diAMP-BCM nanohybrids with a morphology and particle distribution similar to those of BCM nanoparticles as well as a loading capacity of 0.6 ± 0.1% (μg diAMP/μg BSA) (Fig. 4K, L). By measuring the hydrodynamic diameters of diAMP-BCM, we found that the diAMP-BCM maintained ~ 80 nm in the serum (Supplementary Fig. 5). The hydrodynamic diameters are larger than that calculated in the TEM images, which is the results of the thick hydration layer formed from BSA, it also the reason that the particles in the TEM images disperse evenly. Coculturing BMDMs with diAMP-BCM significantly increased the expression of the main inflammatory genes of BMDMs, such as *CXCL10* and *IFNB1*, while the expression of *TNFa* and *IL6* remained unchanged (Fig. 4M). This indicates that the loading of diAMP also promotes the activation of the type I interferon response and does not activate the expression of protumor genes.

Then, we conducted transcriptome sequencing to evaluate the effect of diAMP-BCM on the RNA landscape of BMDMs extracted from mice. Different landscapes were observed in the heatmap showing the gene expression patterns of the BMDMs treated with diAMP-BCM compared with those of the other groups treated with LPS/IFN, diAMP, and BCM (Fig. 4N). Subsequently, protumor-related inflammatory genes and antitumor-related inflammatory genes were extracted from the RNA sequencing results, and the results indicated a decrease in the expression of *IL6*, *TNF*, etc., while the expression of *CXCL10* and *IRF7* increased in the BMDMs treated with diAMP-BCM (Fig. 4O). KEGG analysis also indicated that diAMP-BCM treatment mainly regulated genes related to the NF-kB signaling pathway in a manner opposite to that of LPS/IFN (Fig. 4P, Q). These findings demonstrated that diAMP-BCM suppressed the activation of NF-kB signaling.

The preferential activation of the type I interferon response mediated by diAMP-BCM in BMDMs was indirectly supported by the inhibition of EGFR dampening the expression of genes related to type I interferon activation (Fig. 4R, S) [34]. After the introduction of sorafenib, an EGFR inhibitor, the increased expression of *CXCL10* and *IFNB1* decreased to the control level. EGFR mediates the translocation of STING to late endosomes, which is a critical process that promotes the activation of the type I interferon response. When EGFR was inhibited, the expression of *CXCL10* and *IFNB1* in diAMP-BCM-treated BMDMs did not increase, indicating that the activation of the type I interferon response by diAMP-BCM is dependent mainly on the translocation of STING to late endosomes. The underlying mechanism still needs further investigation.

Furthermore, by establishing CT26 CRC models in BALB/c mice, we evaluated the potential of diAMP-BCM to inhibit CT26 CRC growth in vivo. Tumor regression was observed in the group treated with diAMP-BCM, and 3 in 5 of the tumor-bearing mice were eliminated (Fig. 4T). Notably, the tumors in the group treated with BCM grew faster than those in the control group. When tumor-bearing mice were treated with diAMP-BCM (i.t.) combined with sorafenib (i.p.), tumor regression mediated by diAMP-BCM was inhibited (Fig. 4U).

diAMP-BCM also preferentially activated antitumor inflammatory signaling in BMDCs and T cells

As diAMP is a STING agonist, STING activation is a prevailing signaling pathway in DCs that promotes DC maturation and generates a type I interferon response. While comparing with LPS, the portions of mature DCs after treated by free diAMP are almost equal to the control group, which is much lower than the group treated by LPS (Supplementary Fig. 6). It indicates that the free diAMP has little effect onto the stimulation of DCs maturing. Studies have demonstrated that Mn has the potential to stimulate the cGAS-STING pathway,

which further induces DC maturation and TAM polarization. We first evaluated the effects of the ionic forms of Mn and Cu on the maturation of DCs stimulated by a STING agonist. No obvious enhancement of DC maturation was detected by flow cytometry. More importantly, even in the presence of diAMP, no enhanced DC maturation was observed as the amount of metal ions increased. This finding indicated that the extracellular ionic forms of Mn and Cu cannot efficiently stimulate the activation of STING (Fig. 5A, B). Therefore, a delivery system was introduced not only for ions but also for STING agonists. Compared with the ionic forms of Mn/Cu alone, the BCM nanoparticles not only promoted the maturation of DCs but also enhanced the potential of diAMP to stimulate DC maturation (Fig. 5B). More interestingly, as either the Cu content or the diAMP content increased, the proportion of mature DCs increased (Fig. 5B, C). Although an increase in Mn content favors further stimulation of DC maturation, the adverse effect of Mn ions impedes the application of these nanoparticles in vivo. After stimulation, the morphology of the BMDM-derived DCs expanded, and

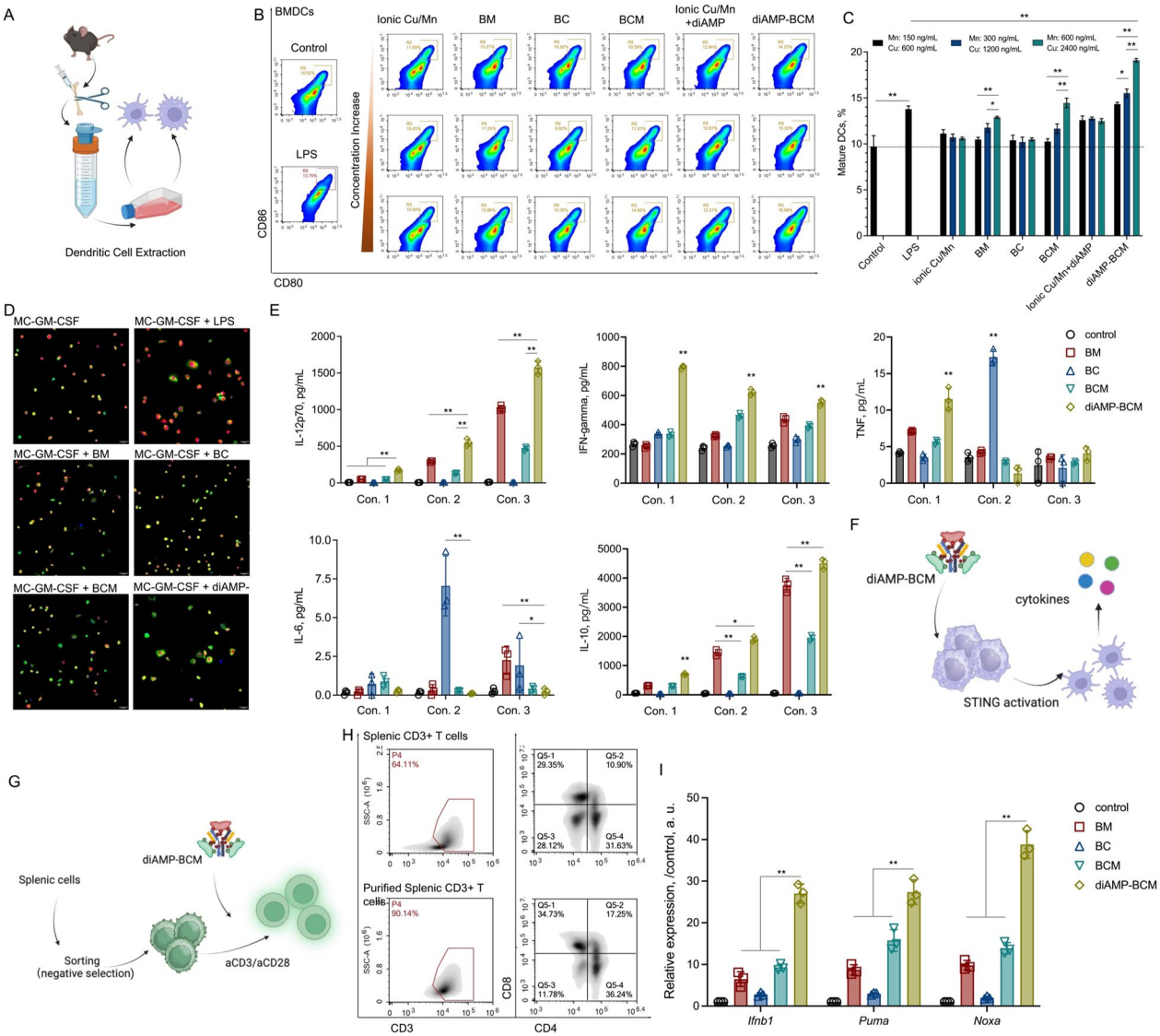

Fig. 5 **A** The extraction and in vitro culture of BMDCs and BMDMs. **B**, **C** Flow cytometry results of BMDM-derived DCs after different treatments. **D** Fluorescence images of BMDM-derived DCs after different treatments. Con.1, Con.2, and Con.3 represent different concentrations of Mn and Cu. **E** Quantitative analysis of CD80+CD86+ DCs measured in **E**. **F** DiAMP-BCM promotes the production of proinflammatory cytokines by APCs. **G** diAMP-BCM promotes the activation of T cells. **H** Isolated splenic CD3+ T cells. **I** qPCR results showing *Ifnb1*, *Puma* and *Noxa* expression in T cells after treatment with diAMP-BCM

promoted pseudopod formation was observed with the introduction of diAMP (Fig. 5D).

Moreover, we further evaluated cytokine levels, which are the result of DC maturation after STING activation, in the supernatant of BMDM-derived DCs after coculturing with different formulations. The concentrations of IL-12p70, TNF, IFN-gamma and IL-6 were dramatically increased in the BM-treated BMDCs, while diAMP-BCM-treated DCs exhibited decreases in IL-6 and TNF and increases in IL-12p70 and IFN-gamma (Fig. 5E). Moreover, the IL-10 level was also apparently upregulated in the supernatant of the cells treated with diAMP-BCM in a dose-dependent manner (Fig. 5E). The upregulation of IL-10 is the result of negative feedback, while inflammation and maturation are induced in cells, and some reports also indicate that IL-10 favors the enhancement of antitumor immunity. These results further indicate that diAMP-BCMs exhibit the potential to induce the maturation and polarization of APCs, especially DCs and macrophages, to generate proinflammatory cytokines (Fig. 5F).

Furthermore, we isolated CD3+ T cells from splenumentally extracted cells by negative selection via a mouse CD3+ T-cell isolation kit. Then, the cells were stimulated with aCD3/aCD28 for several days (Fig. 5G, H). Then, the stimulated CD3+ T cells were cocultured with different BCM formulations. Gene levels related to postactivation of STING were measured by RT-qPCR. The upregulation of *Ifnb1*, *Puma*, and *Noxa* was clearly observed in the cells treated with diAMP-BCM (Fig. 5I). These findings indicate that diAMP-BCM also efficiently stimulates the activation of CD3+ T cells via the STING pathway.

DiAMP-BCM facilitates the recruitment and differentiation of monocytes by inducing the apoptosis/pyroptosis of CRC cells

Although diAMP-BCM has exhibited great potential in regulating the behavior of APCs, recruitment of APCs to the tumor site favors the long-lasting regulation of antitumor immunity. Cancer cell apoptosis, particularly pyroptosis, promotes the recruitment of monocytes to tumors, and the recruited monocytes can be differentiated to a proinflammatory phenotype by diAMP-BCM to inflame the TiME. Thus, we first conducted cellular cytometry assays and CCK8 assays to evaluate the cytotoxicity of diAMP-BCM and its potential to induce tumor cell apoptosis/pyroptosis. The CT26 and MC38 CRC cell lines were used. As the diAMP-BCM concentration increased, a dramatic decrease in cancer cell survival was observed, and the IC50 of diAMP-BCM for CT26 cells was ~ 1.25 μg diAMP (Fig. 6A). No obvious apoptosis was observed in the group treated with diAMP alone, and the apoptosis of the CT26 cells treated with diAMP-BCM was similar to that of the cells treated with BCM (Fig. 6B). However, the cellular morphology after diAMP-BCM treatment indicated that pyroptosis also occurred (Fig. 6C). The percentage of surviving cells at this concentration of diAMP-BCM was approximately 0%, which is also inconsistent with the percentage of apoptotic cells (only ~ 14%). This indicates that most cancer cell death may be the result of pyroptosis.

In the case of MC38 CRC cells, by apoptosis assay evaluation, we found that high percentages of early apoptosis and late apoptosis were both observed in MC38 cells treated with BCM, and the percentages further increased in the presence of diAMP, in which the percentage of total apoptotic cells reached ~ 60%, which was much greater than that in the BCM-treated group (Fig. 6D). The potential of diAMP-BCM to induce tumor apoptosis was dose dependent (Fig. 6E and Supplementary Fig. 7). As a consequence, diAMP-BCM efficiently inhibited the growth and proliferation of tumor cells in vitro. The apoptosis results were consistent with those of the CCK-8 assays performed in the MC38 cell line (Fig. 6F). The potential anticancer effect of diAMP-BCM was further supported by the inhibition of MC38 growth in vivo. After intratumoral injection, the tumors treated with diAMP-BCM regressed within 12 days, and 4 in 5 of the tumor-bearing mice were eliminated (Fig. 6G, H). Notably, the tumors treated with BCM nanoparticles alone all tended to progress, with significantly larger average tumor volumes than those in the control group (which indicates that hyperprogression occurred) (Fig. 6G, H).

The apoptosis or pyroptosis of cancer cells may promote the recruitment of monocytes, which can be differentiated into macrophages or DCs. After one intratumoral injection, the dose of diAMP was decreased to 5 μg per mouse (Fig. 6I). On day 3, monocytes, as well as DCs, were obviously recruited to the diAMP-BCM-treated tumors. These findings indicate that diAMP-BCM promotes the recruitment of monocytes (Fig. 6J, K). The recruitment of monocytes was mainly ascribed to the apoptosis of tumor cells caused by Cu and STING via the Fenton reaction and STING pathway activation. As previously reported, the recruited monocytes can differentiate into TAMs in the immunosuppressive TME, and the differentiated TAMs further aggravate the immunosuppressive TiME, thus promoting the exhaustion of T cells. By extracting and deriving monocytes from the bone marrow, BMDMs were differentiated directly by diAMP-BCM in vitro. The results indicated that proinflammatory phenotypes were induced in the extracted

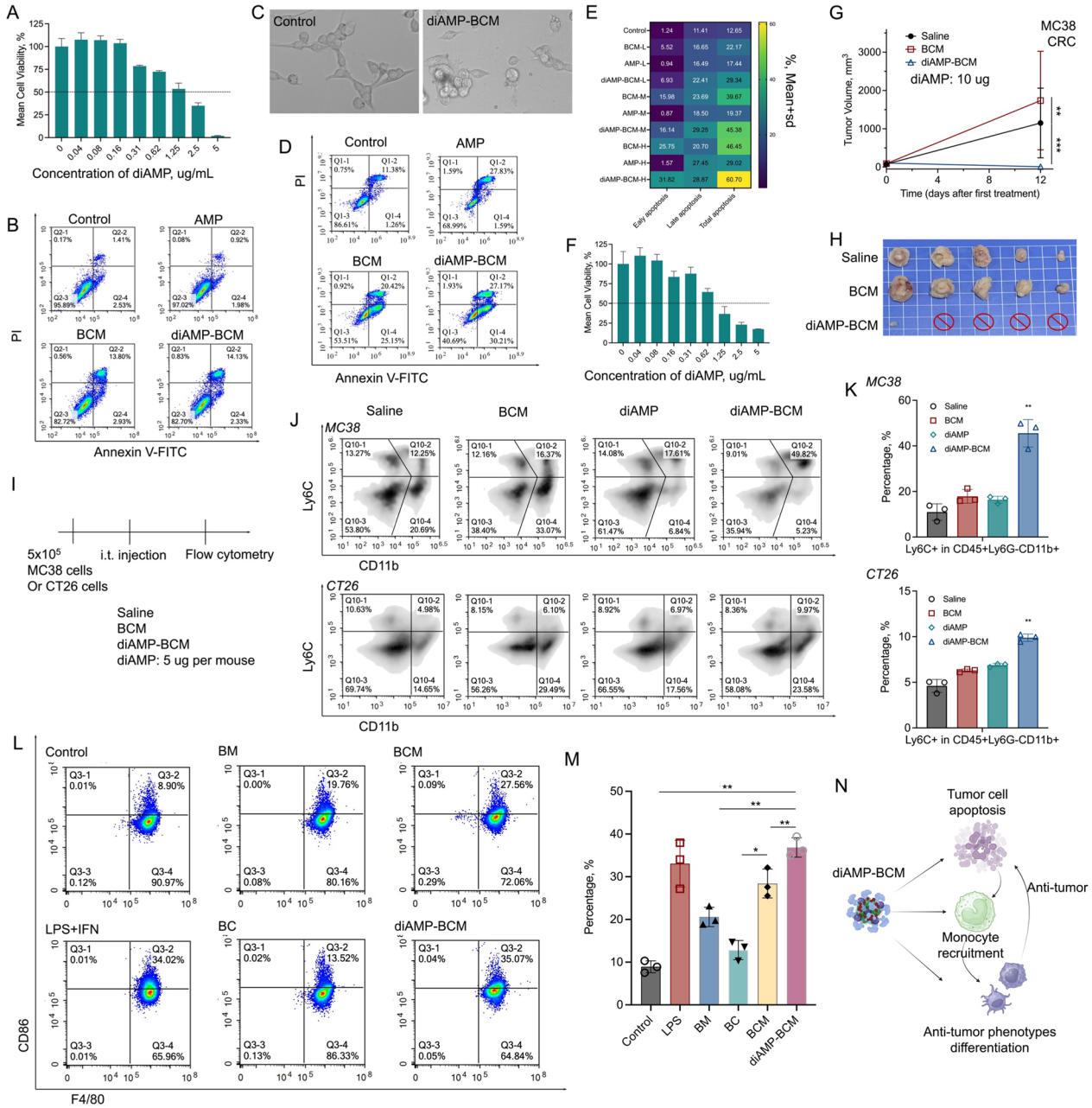

Fig. 6 diAMP-BCM promotes the recruitment and differentiation of monocytes. **A** Survival of CT26 cells treated with diAMP-BCM. **B** Apoptosis and **C** optical images of CT26 cells after treatment with diAMP-BCM. **D**, **E** The apoptosis of different BCM-treated MC38 cancer cell lines was measured by flow cytometry. **F** The survival of MC38 cells treated with diAMP-BCM (measured by a CCK-8 assay). **G**, **H** In vivo growth inhibition of MC38 cancer cells by diAMP-BCM. **I** Illustration of the evaluation of monocyte recruitment by diAMP-BCM. **J**, **K** Populations of intratumour monocytes in MC38 CRC and CT26 CRC mice after different treatments, respectively. **L**, **M** The proportions of F4/80+CD86+ bone marrow-derived cells (BMDCs) after different treatments were measured by flow cytometry. Mn: 0.3 μg/mL, Cu: 1.2 μg/mL, diAMP: 1 μg/mL. BMDCs were extracted from the bone marrow of mice and stimulated with M-CSF. **N** diAMP-BCM regulates versatile cell behavior to enhance tumor inhibition

BMDMs via the features of M1 macrophages (Fig. 6L, M). These findings demonstrated that diAMP-BCM itself can promote the differentiation of monocytes to proinflammatory phenotypes with antitumor effects in vivo (Fig. 6N).

DiAMP-BCM reshaped the TiME landscape to "hot" tumors during aPD-1 ICB therapy for CRC

It has been demonstrated that the main therapeutic effects of aPD-1 therapy in vivo are mainly related to T-cell exhaustion and the recruitment of new peripheral

T cells from circulation or from tumor-draining lymphatic nodes (TDLNs) [6]. The decrease in tumor-resident CD4+ T cells and CD8+ T cells and the subsequent recruitment of T cells may favor the enhancement of aPD-1 therapy and remodeling of the tumor immune microenvironment. Here, we investigated the effect of diAMP-BCM on the TiME and the potential of diAMP-BCM combined with aPD-1 to rebuild the lymphocytic microenvironment via transcriptome sequencing of mouse tumors after different treatments. Significantly different transcriptional landscapes were observed in the diAMP-BCM- and diAMP-BCM+aPD-1-treated groups compared with the other groups (saline-, BM-, and BCM-treated groups), particularly in the diAMP-BCM+aPD-1-treated groups (Fig. 7A). More than 1200 genes were upregulated in the tumors of mice treated with diAMP-BCM+aPD-1, which was much greater than the number of upregulated genes in the tumors of mice treated with diAMP-BCM (Supplementary Fig. 8). This finding indicated that the introduction of aPD-1 further reshaped the TiME. By Gene Ontology (GO) and Kyoto Encyclopedia of Genes and Genomes (KEGG) enrichment analyses (Fig. 7B–E), we found that the combination of diAMP-BCM and aPD-1 promoted the stimulation of immune responses, as the DEGs were mainly associated with immune responses, and genes related to "PD-L1 expression and the PD-1 checkpoint pathway in cancer" were also found to be upregulated.

Additionally, genes related to pyroptosis, mast cell (MC) recruitment, inflammation, B-cell recruitment, NK cell/T-cell recruitment, T-cell activation, and tertiary lymphoid structure (TLS) formation were significantly upregulated in the diAMP-BCM+aPD-1-treated group, while only genes related to MC recruitment,

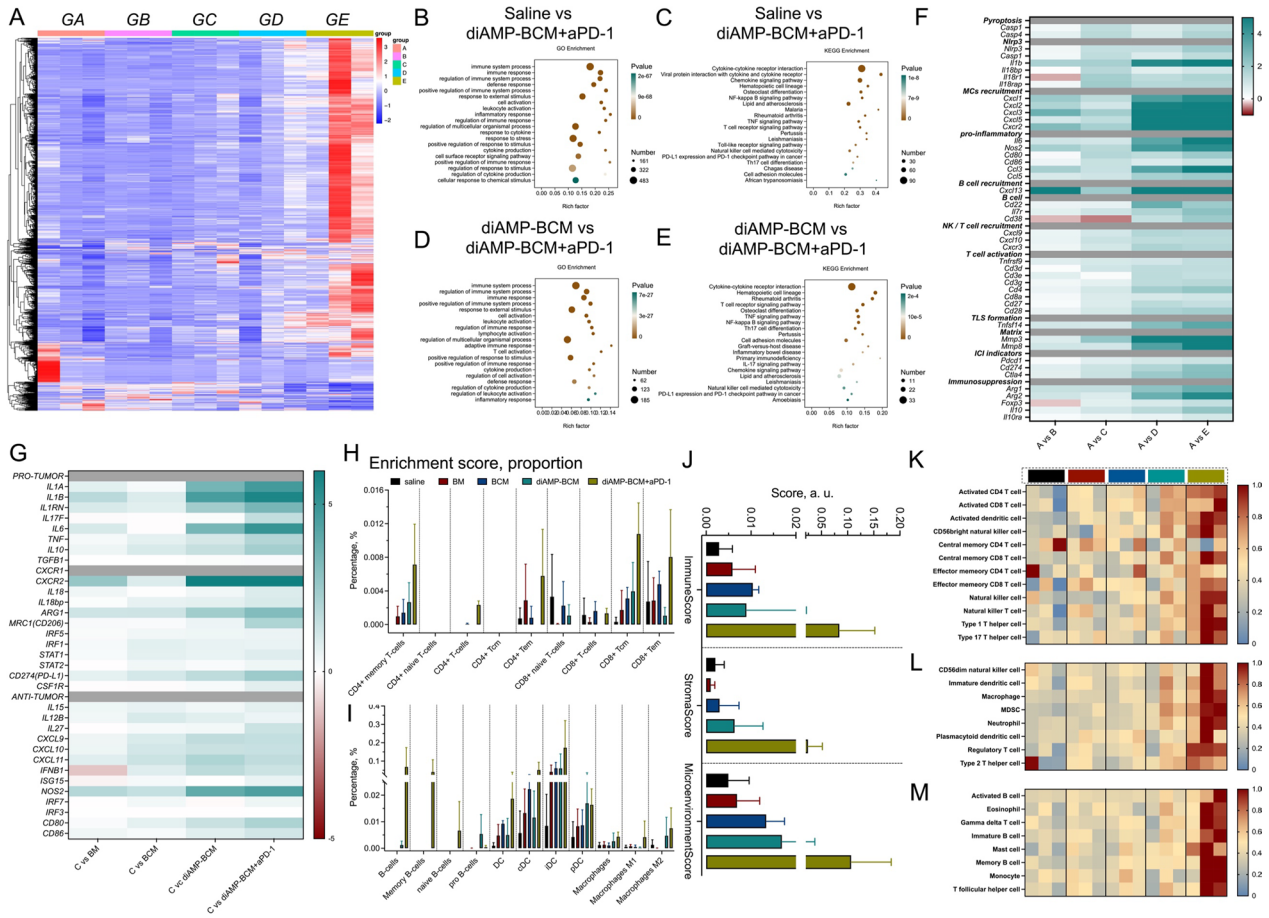

Fig. 7 The underlying mechanism deduced from the transcriptome sequencing of whole MC38 tumors after different treatments. **A** Heatmap of the transcriptome sequencing results of whole tumors after different treatments. (GA: control, GB: BM, GC: BCM, GD: diAMP-BCM, GE: diAMP-BCM+aPD-1, G = group). **B**–**E** GO enrichment analysis (**B**, **C**) and KEGG enrichment analysis (**D**, **E**) of the transcriptional landscape of tumors treated with diAMP-BCM (**B**, **D**) and diAMP-aPD-1 (**C**, **E**). **F** Gene expression representing different cellular behaviors of tumors after different treatments. **G** Heatmap of the expression of the main genes related to inflammation, including protumor and antitumor genes. **H**–**J** xCELL analysis revealing immune infiltration of tumors after different treatments. **K**–**M** ssGSEA revealed differences in the TiME of the tumors after different treatments

inflammation, and TLS formation were upregulated in the diAMP-BCM-treated group. Genes related to immune checkpoint indicators and immunosuppression were also upregulated in the diAMP-BCM+aPD-1-treated group, indicating feedback regulation of the immune system. (Fig. 7F). Furthermore, unlike the results obtained for BMDMs in vitro, the expression of IL6 and TNF in tumor tissues was still significantly increased after diAMP-BCM treatment, particularly during aPD-1 ICB therapy. These findings indicate that other cell types beyond APCs overexpress protumor inflammatory genes, e.g., IL6 and TNF. According to the cytotoxicity results of diAMP-BCM to cancer cells, pyroptosis may occur when cancer cells are treated with diAMP-BCM. Pyroptosis of cancer cells can also promote the expression of pro-tumor inflammatory cytokines, including IL6, TNF, and IL1, which are all overexpressed in tumor tissues treated with diAMP-BCM with or without aPD-1 therapy (Fig. 7F, G).

Using xCELL and immuneCC analyses, we found that the proportions of $CD8^+$ T cells and $CD8^+$ effector memory T (Tem) cells were significantly decreased in the group of mice treated with diAMP-BCM alone. With the introduction of aPD-1, the proportions of $CD8^+$ T cells and CD8+ Tem cells as well as the proportion of $CD8^+$ central memory (Tcm) cells increased (Fig. 7H). These changes were accompanied by a synchronous increase in the number of B cells and APCs, including DCs and macrophages (Fig. 7I). The immune score, stroma score and microenvironment score also indicated that the introduction of aPD-1 changed the TiME (Fig. 7J). Similar results were obtained by single-sample gene set enrichment analysis (ssGSEA), which revealed a marked increase in the proportion of effector T cells and their related immunocytes (Fig. 7K–M).

The diAMP-BCM enhances the efficacy of CRC ICB (aPD-1) immunotherapy in vivo

To evaluate the potential of diAMP-BCM combined with aPD-1 to remodel the TiME and increase the efficacy of immunotherapy, we further assessed the effect of diAMP nanoparticles (diAMP-BM, diAMP-BC, and diAMP-BCM with different Cu/Mn ratios) on ICB CRC immunotherapy. During the administration of aPD-1, the growth of MC38 cells was inhibited in vivo. However, without continuous administration of aPD-1, the growth of MC38 cells was similar to that of the control group (Supplementary Fig. 9). With the introduction of diAMP-BCM, tumor growth was obviously inhibited, and regression was observed in some of the tumors. At the same dose of either Mn or Cu, the tumor growth inhibition in the groups treated with diAMP-BM or diAMP-BC was significantly inferior to that in the diAMP-BCM-treated group, although moderate tumor growth inhibition was achieved by these treatments. In addition, the results indicated that the Cu/Mn ratio critically affects the therapeutic outcome of ICB. As the Cu/Mn ratio increased from 0.25/1 to 1:1, the average volume and tumor weight increased, although there were no significant differences between these two groups. As the Cu/Mn ratio further increased (Fig. 8A–C). This finding demonstrated that Cu/Mn-based treatment enhanced the therapeutic efficacy of ICB when combined with a STING agonist and that the therapeutic efficacy can be regulated by the Cu/Mn ratios within the nanoparticles.

Then, we further evaluated the effects of different treatments on the TiME, particularly on macrophages and immunocytes, by immunofluorescence staining of tumor sections (Fig. 8D). Both the groups treated with diAMP-BM+aPD-1 and diAMP-BCM+aPD-1 (Cu/Mn = 4:1) exhibited an increased proportion of F4/80+CD86+ macrophages, which are considered proinflammatory, or M_1 macrophages. Moreover, these two groups also exhibited a decrease in the proportion of $F4/80^+CD206^+$ macrophages. This finding indicated that the TiME remodeled to a proinflammatory state in response to these two treatments. Notably, the group treated with diAMP-BC+aPD-1 exhibited an increased proportion of $F4/80^+CD206^+$ macrophages. More importantly, the proportion of $CD3^+CD8^+$ T cells was much greater than that in the other group, and this T-cell phenotype was rare in the diAMP-BCM+aPD-1 (Cu/Mn = 4:1)-treated group. However, the diAMP-BCM+aPD-1 (Cu/Mn = 4:1)-treated group had a significantly greater number of $CD3^+$ cells surrounding the tumor (Fig. 6D). This finding indicated that diAMP-BCM+aPD-1 (Cu/Mn = 4:1) decreases the proportion of $CD3^+CD8^+$ T cells but promotes the recruitment or cloning of $CD3^+$ cells in the initial period after treatment.

diAMP-BCM combined with ICIs facilitates distal tumor management and alleviates distal T-cell exhaustion

This study demonstrated that diAMP-BCM promoted the rebuilding of the tumor lymphocytic microenvironment and increased the efficacy of immunotherapy, which indicated the potential of this strategy for inhibiting the growth of distal tumors. CRC normally occurs in multiple areas. It is necessary to establish a CRC therapeutic strategy to inhibit distal tumors. Therefore, we established an MC38 tumor model on both flanks of C57BL/6J mice simultaneously; only the tumors on the right side were intratumorally injected with diAMP-BCM, and all of the mice except the control mice were subsequently intraperitoneally injected with aPD-1 (Fig. 9A). The volumes of the tumors on both sides were recorded. The most

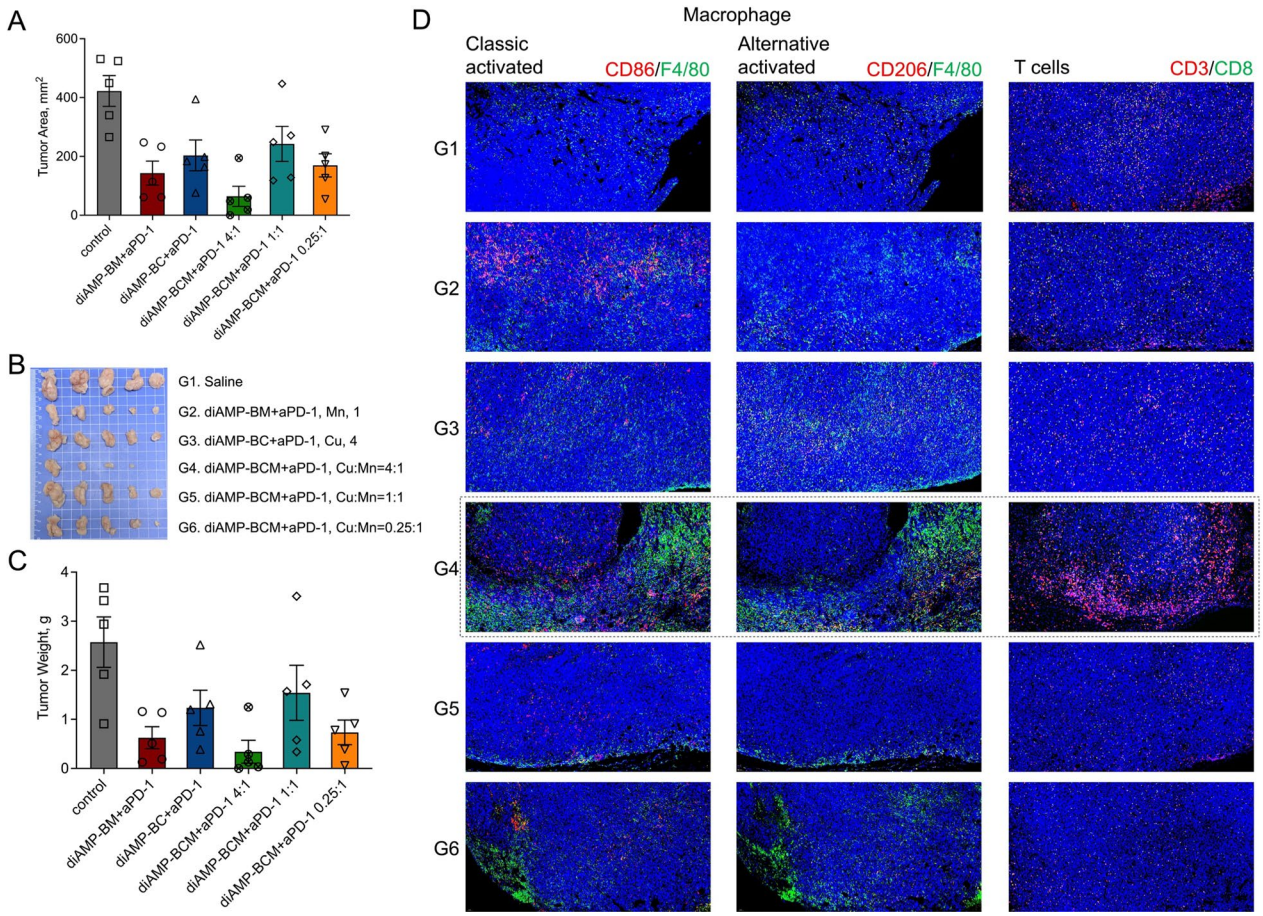

Fig. 8 Tumor growth inhibition of diAMP-BCMs in combination with aPD-1 in vivo and effects on the TiME. **A** The tumor area of MC38 tumors implanted in C57/B6J mice after different treatments. **B** Photograph of the tumors ex vivo at the endpoint of the treatments. **C** The tumor weights ex vivo at the endpoint of the treatments. **D** Immunofluorescence images of the tumors after different treatments in which the immunocytes and APCs were labeled

efficient tumor growth inhibition was observed in the group treated with diAMP-BCM+aPD-1, which inhibited the growth of not only the treated right-sided tumors but also the treated distal left-sided tumors (Fig. 9B–D). Tumor progression was slightly inhibited in the group treated with diAMP+aPD-1, but the tumor growth in this group was far faster than that in the diAMP-BCM+aPD-1-treated group. This finding revealed that BCM has a synergistic effect with ICB immunotherapy. Then, we evaluated the effect of combination therapy on the TiME of tumors on the treated side and the distal nontreated side. An obvious increase in the proportion of F4/80+CD11c+ cells was observed in the group treated with diAMP-BCM+aPD-1 in both the treated tumors and distal tumors (Fig. 9E, H). Similar results regarding the proportions of $CD3^+CD8^+$ T cells were obtained (Fig. 9F, I). More importantly, by further staining for the exhausted T-cell markers PD-1 and TIM-3, we found that the proportion of $CD3^+CD8^+PD\text{-}1^+TIM3^+$ T cells in distal tumors dramatically decreased in the group treated with diAMP-BCM+aPD-1, while the proportion of $CD3^+CD8^+PD\text{-}1^+TIM3^+$ T cells on the treated side did not significantly differ (Fig. 9G, J). The results of multiplex immunohistochemistry (mIHC) staining of tumor slices of distal tumors further revealed a decrease in exhausted T cells with enhanced enrichment of $CD3^+CD8^+$ T cells and $CD3^+CD8^+TCF1^+$ T cells (Fig. 9K, L). Further investigation of the tumor tissues obtained 3 days after the final intratumor injection revealed enhanced monocyte enrichment in the group treated with diAMP-BCM+aPD-1 (Supplementary Fig. 10), with an increase in CD3+CD8+ T cells, indicating the expansion of effector T cells; moreover, in both the treated tumors and the distal tumors, a decrease in the proportion of $CD3^+CD8^+PD\text{-}1^+TIM3^+$ T cells was also observed in this group (Supplementary Fig. 11 and Supplementary Fig. 12). We also found

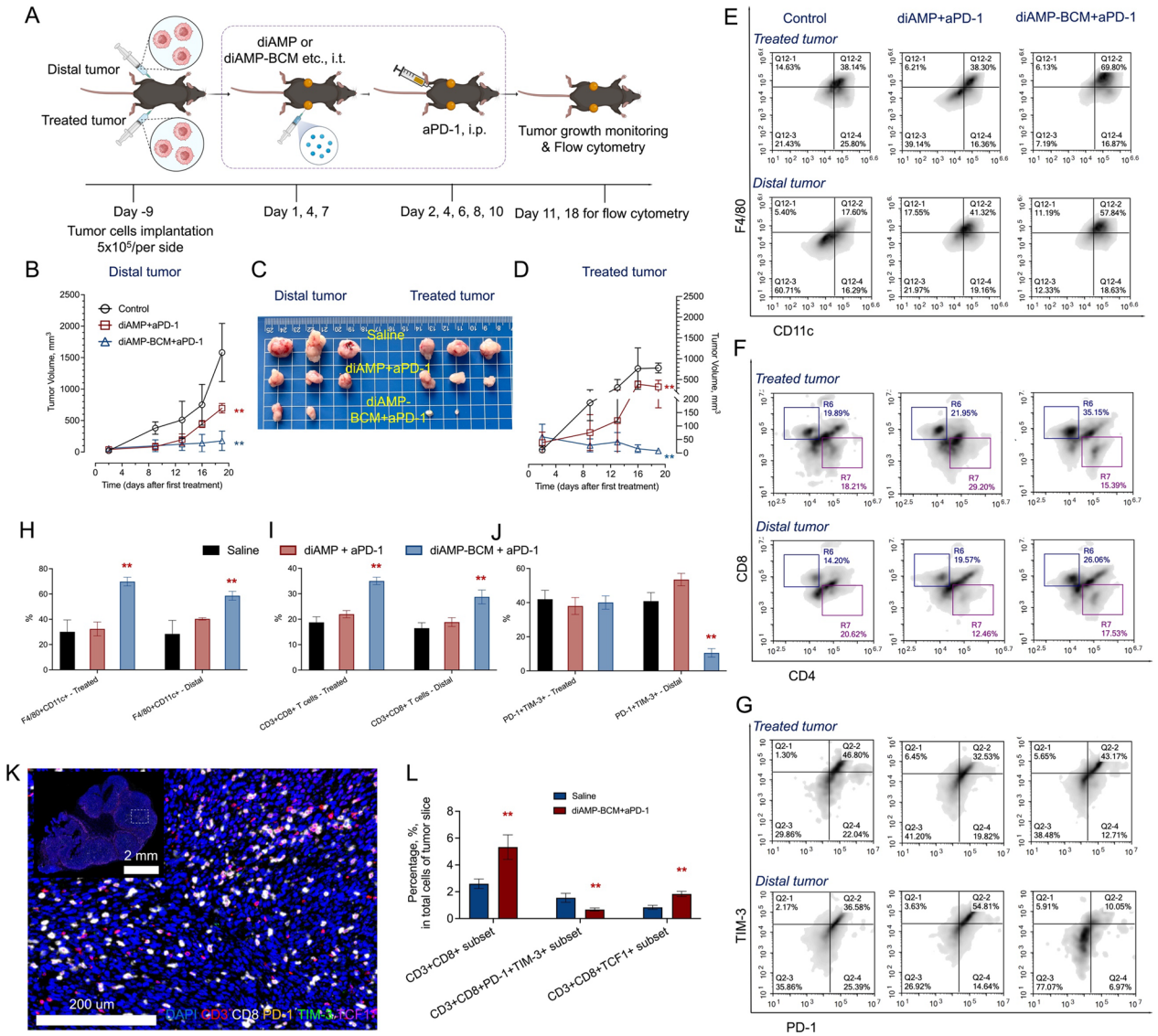

Fig. 9 Effect of diAMP-BCM combined with aPD-1 on the growth inhibition of distal tumors and the underlying immune response. **A** Schematic illustration of tumor growth inhibition in distal tumor models. **B**–**D** Tumor volume variation after different treatments (**B**, **D**) and ex vivo images of the tumors. **E** The proportions of F4/80+CD11c+ macrophages in the treated and distal tumors after different treatments. **F** Populations of CD3+CD4+ and CD3+CD8+ T cells in the treated and distal tumors after different treatments. **G** The percentages of exhausted T cells in the tumor tissues were measured by flow cytometry. **H**–**J** Statistical analysis of the percentages of $F4/80^{+}CD11c^{+}$ T cells, $CD3^{+}CD8^{+}$ T cells, and $CD3^{+}CD8^{+}PD\text{-}1^{+}TIM3^{+}$ T cells in treated tumors and distal tumors. **K** mIHC fluorescence image of tumor slices from distal tumors after treatment with diAMP-BCM+aPD-1. **L** The proportions of different lymphocytes calculated from the mIHC images

that the proportion of $CD3^{+}CD8^{+}PD\text{-}1^{+}TIM3^{+}$ T cells in the spleens of the mice treated with diAMP-BCM+aPD-1 was lower than that in the other groups (Supplementary Fig. 13). In the initial period, diAMP-BCM+aPD-1 not only promoted the expansion of effector T cells but also alleviated T-cell exhaustion in both primary tumors and distal tumors.

Discussion

Colorectal cancer (CRC) is a fatal cancer with high morbidity and mortality. Although ICB has provided a promising option for efficient inhibition of CRC, only a small portion of patients benefit from this approach. Most CRC patients with pMMR/MSS features have a low or even no response, while more than 30% of dMMR/MSI-H CRC patients are resistant (primary or acquired) to ICB therapy [3, 35, 36]. Converting the "cold" TiME

to a "hot" milieu has become the prevailing strategy for enhancing the response of CRC to ICB therapy. However, a "hot" TiME is generally accompanied by aggravated inflammation and versatile chemokines/cytokines. Some chemokines/cytokines, e.g., TNF and IL-6, have been demonstrated to play a role in promoting cancer progression. In addition, inflammation is also considered the main cause of resistance to ICB therapy in dMMR/MSI-H CRC patients [8]. Therefore, strategies that preferentially activate antitumor inflammatory signaling, rather than protumor signaling, need to be developed to enhance the effectiveness of CRC ICB therapy.

Because ROS are the main driving force and main promoter involved in the formation and progression of inflammation, metal-based nanoparticles with intracellular catalytic performance are promising candidates for the regulation of inflammation. Thus, we first prepared BC and BM nanoparticles. These catalysts exhibited excellent catalytic properties, as expected. More importantly, by adjusting the ratio of BC and BM nanoparticles, diverse activation intensities of macrophages were observed, indicating that the BC/BM ratio controls the activation of macrophages.

By in vitro assessment, we confirmed the potential of BCM nanosystems to stimulate the production of ROS. We further adsorbed diAMP into the BCM structure and obtained diAMP-BCM nanohybrids. diAMP-BCM promoted the polarization of RAW264.7 cells to a pro-inflammatory phenotype. We also found that diAMP-BCM nanoparticles upregulated the expression of *IRF7* and *CXCL10* while decreasing the expression of *TNF, IL6*, etc. The enhanced expression of IRF7 and production of CXCL10 indicate the activation of the type I interferon response, which promotes antitumor immunity [37]. TNF-α and IL6 are considered indicators of the activation of protumor inflammatory signaling. The results demonstrated that diAMP-BCM achieved the primary goal of this study. Furthermore, apoptosis and pyroptosis were observed in diAMP-BCM nanocomplex-treated MC38 cells and CT26 cells. In situ treatment of tumors with diAMP-BCM can not only promote the recruitment of monocytes but also favor the differentiation of recruited monocytes to proinflammatory phenotypes instead of TAMs [38, 39].

In combination with aPD-1, diAMP-BCM nanohybrids reshape the TiME. With the combination of ICB therapy, diAMP-BCM seemed to induce the formation of TLSs, which was supported by the overexpression of markers related to B-cell recruitment (*CXCL13*) and high endothelial venule (HEV) formation (*TNFSF14*) as well as T/NK cell recruitment (*CXCL9/CXCL10*). TLSs serve as important control centers for the recruitment of immunocytes and the induction of their differentiation, and in several cancer cell types, the formation of TLSs is positively correlated with the prognosis of cancer patients [40–42]. Moreover, *MM3* and *MMP8* were also upregulated in the group treated with diAMP-BCM combined with ICB. These parameters are also considered indicators of a positive prognosis [43–45]. By xCELL and immuneCC analysis as well as ssGSEA of the transcriptional profiles of the tumor tissues after different treatments, we found that the diAMP-BCM combined with ICB treatment group exhibited the highest immune score and microenvironment score [46, 47], further demonstrating that the therapeutic outcome of the combination therapy is the consequence of TiME regulation.

Moreover, the potential of diAMP-BCM combined with ICB to remodel TiME could be regulated by the ratios of the metals due to their ability to regulate cell behavior. According to the results of the in vivo MC38 CRC model experiment, without other interventions, BM alone resulted in an inflammatory microenvironment that promoted the progression of tumors. However, the Cu-based nanosystem induced apoptosis in tumor cells via ROS generation, which indicated that Cu can facilitate macrophage polarization to an anti-inflammatory phenotype. By adjusting the ratios of Cu/Mn in diAMP-BCM, we can maximize tumor growth inhibition while combining diAMP-BCM with aPD-1. This finding indicates that diAMP-BCM favors minimizing the influence of the immunosuppressive TiME on recruited T cells and instead promotes the differentiation of milieus-like T cells to effector T cells, which enhances the efficacy of ICB.

The final but most critical factor is that immune stimulation by diAMP-BCM combined with ICB immunotherapy can also promote the inhibition or even regression of distal CRC. CRC is characterized by dissemination and multiple loci. Enhancing the inhibition of distal tumors is critical. In the distal tumor model, the primary tumors of diAMP-BCM+aPD-1-treated mice regressed, while the growth of distal tumors was also inhibited and appeared to be in remission. By further analyzing the lymphocytic microenvironment after different treatments, the expansion of CD3+CD8+ T cells was indicated by the increase in the proportion of $CD3^+CD8^+$ T cells in the diAMP-BCM+aPD-1-treated group on day 3 or day 8 after the final intratumoral injection. This indicates that the introduction of aPD-1 changes the potential of diAMP-BCM to regulate the lymphocytic microenvironment. Moreover, diAMP-BCM+aPD-1 treatment reduced the proportion of $CD3^+CD8^+PD\text{-}1^+TIM3^+$ T cells in both the treated tumors and distal tumors and in the spleen on day 3. However, on day 8, the proportion of $CD3^+CD8^+PD\text{-}1^+TIM3^+$ T cells in the treated tumors

increased, while that in the distal tumors remained low. $CD3^+CD8^+PD\text{-}1^+TIM3^+$ T cells can be considered exhausted T cells, which make up a large number of intratumoral T cells and are positively correlated with poor patient prognosis in some cancer types [48, 49]. Although some recent studies have indicated that exhausted T cells still maintain antitumor activity, strategies have been developed to reactivate exhausted T cells, particularly exhausted T-cell progenitors. In addition, newly recruited tumor-infiltrating T cells are still exposed to the immunosuppressive TME, which completely impairs the effector functions of T cells shortly (24 h) after the recruited T cells encounter the TME [50, 51]. Therefore, strategies that efficiently remodel the TiME to promote effector T-cell function could be promising for enhanced ICB therapy [52]. We demonstrated that diAMP-BCM+aPD-1 can efficiently alleviate T-cell exhaustion, and treatment of tumors with diAMP-BCM combined with aPD-1 resulted in excellent tumor inhibition in both treated tumors and distal tumors.

In summary, we constructed a STING agonist-loaded bimetallic nanosystem, termed diAMP-BCM. BCM with an optimized Cu/Mn ratio efficiently promoted the activation of proinflammatory signaling, and in combination with the STING agonist diAMP, the diAMP-BCM nanohybrids controllably activated inflammatory signaling, reinforcing antitumor immunity. DiAMP-BCM can efficiently generate ROS and promote the activation of STING, which induces the apoptosis of cancer cells and promotes the recruitment of monocytes while facilitating the polarization of macrophages and maturation of DCs. Combined with ICB therapy, diAMP-BCM enables the rebuilding of tumor milieus with efficient tumor growth inhibition and alleviation of T-cell exhaustion, particularly in distal tumors in the long term. Although this nanosystem is still facing that the limitation of intratumoral injection, some state-of-the-art technique for effectively systematic delivery of the therapeutics have been developed [53–55]. These systems provide potential options to address this issue. This study established a nanoplatform to promote the activation of antitumor inflammatory signaling pathways and rebuild the T-cell repertoire to enhance cancer immunotherapy combined with ICIs. Although further investigations need to be performed in other cancer models with different pathological classifications, this approach provides an alternative strategy to remodel the TiME and alleviate T-cell exhaustion.

Methods and materials

Materials

The chemical and biological reagents used in the study are listed in Supplementary Table 1.

All animal procedures were performed following protocols approved by the Institutional Animal Care and Treatment Committee of Sichuan University (Chengdu, P. R. China) and West China Hospital, Sichuan University. The cell cultures were maintained in an incubator at 37 °C with a humidified 5% CO_2 atmosphere. Mice were kept under specific pathogen-free (SPF) conditions with free access to standard food and water.

Preparation of BCs, BMs, BCMs and diAMP-BCMs

The BCMs were prepared according to our previous reports with some modifications. In brief, a two-step procedure was used to prepare BCM. First, 1 mL of $Cu(NO_3)_2$ HNO_3 solution (0.2 M) was added dropwise to an aqueous solution of BSA (250 mg/mL), and then the mixture was stirred for 30 min at room temperature. Then, the reaction mixture was transferred to an oil bath preheated to 90 °C, and 3 mL of Na_2S solution (0.2 M) was added under stirring. The reaction was maintained for another 30 min before dialysis against distilled water (the cutoff molecular weight was 10 kDa) for 48 h. The obtained dialyzed solution was further lyophilized, and the BC product was kept in a dry and low-temperature environment for further applications.

To further prepare BCM nanoparticles, lyophilized BC powder was first dissolved in distilled water, and then a certain amount of $MnCl_2$ aqueous solution was added and stirred for 10–15 min at RT. NaOH was added, and the reaction was maintained for another 3 h. The pH of the reaction mixture was monitored during the reaction. Similar to the postprocessing procedure, the postprocessing procedure was performed according to that of BC preparation.

The diAMP-BCMs were prepared by mixing the diAMP aqueous solution with a certain amount of BCMs (or BCs, BMs) dissolved in 1×PBS for 2 h at 4 °C. Purification was conducted by ultrafiltration to detect the amount of diAMP in the filtrate to indirectly calculate the loading capacity.

The morphologies of the obtained BCMs, BCs, and BMs were observed by a telescope electronic microscope. The absorption of the nanoparticles was measured by a UV–visible spectrometer. The binding energies of the elements in the nanoparticles were measured by XPS, while the contents of Cu and Mn were detected by ICP–AES after the ions in the nanoparticles were extracted and dissolved in the acidic media.

ROS generation of BCMs

The ROS generation of BCMs can also be estimated by ESR spectroscopy (Bruker EMXnano spectrometer, Germany). The free radical capture agent DMPO was utilized to detect the ·OH generated from the Fenton reaction of CU and Mn with H_2O_2 (2 mM), which presented characteristic peaks in the ESR spectra. Different concentrations of BC, BM and BCM were added, and the ability of the nanoparticles to generate ·OH was indicated by the decrease in the ESR signal.

Intracellular ROS generation in BCMs

To quantify the ROS generation ability of BCMs, RAW264.7 cells and HUVECs were seeded into 6-well plates at densities of 1×10^5 and 1.5×10^5 cells per well, respectively. After 24 h of incubation, the cells were then treated with different concentrations of the BCMs (0–10 μg/mL) and cultured for another 12 h. Next, the Raw264.7 cells were stimulated with LPS (100 ng/mL) for 6 h, and the HUVECs were treated with H_2O_2 (1 mM) for 1 h before being loaded with the DCFH-DA probe (10 μM) for 20 min in the dark. Cells incubated with LPS or H_2O_2 only were used as controls. After washing with FBS-free culture buffer, the levels of cellular ROS were monitored by flow cytometric analysis (NovoCyte Flow Cytometer). To further investigate mitochondrial reactive oxygen species (mitoROS) in live cells reliably, mitoSOX™ probes at a final concentration of 5 μM were added to the aforementioned BCM-treated HUVECs and incubated for 1 h at 37 °C in the dark, followed by flow cytometric analysis. Finally, the viability of the Raw264.7 cells and HUVECs was measured by the MTT assay.

A similar procedure was used to evaluate the mitochondrial membrane potential by JC-1 staining. When the cells were stained with JC-1, after being cocultured with different formulations, the fluorescence of JC-1 was observed by laser scanning confocal microscopy.

Extraction of myeloid cells and induction of DCs and macrophages as well as splenic CD3+ T cells

MC extraction and induction of macrophages and DCs were performed according to standard protocols with some modifications. MCs were extracted from C57/B6J mice and Ai9-LysMcre mice. The thigh bones of these mice were eviscerted after they were euthanized and immersed in 75% ethanol aqueous solution for 10 min. The marrow cells were obtained by repeatedly washing the bone with a syringe containing PBS. Then, the marrow cells were collected by centrifugation and recultured in Petri plates with culture medium supplemented with 10% FBS and stimulating factors (M-CSF, 20 ng/mL for macrophage induction; GM-CSF, 20 ng/mL for dendritic cells). After being cocultured with stimulating factors for several days (5 days for macrophages and 7 days for dendritic cells), the obtained differentiated myeloid cell phenotypes were used for further induction assays.

Effect of BCMs (± diAMPs) on the maturation of GM-CSF-induced DCs

After the BMDMs were induced to differentiate into DCs, BCMs with or without diAMP loading were added to the media to induce DC maturation. Different concentrations of BCMs and diAMPs were investigated. In addition to the BCMs tested, ions (Mn^{2+} and Cu^{2+}) with or without diAMP were also evaluated. After being cocultured for 24 h or 48 h, the cells were collected and washed before immunofluorescence staining for flow cytometry. aCD11c, aCD80, and aCD86 were used to identify the proportion of mature DCs. For morphological observation, the BMDMs extracted from the transgenic mice with red fluorescence were used for better imaging. After coculturing with different formulations (BCMs, diAMP-BCMs, etc.), the DCs were fixed and stained for actin with phalloidine and then washed with 1×PBS three times before being observed by laser scanning confocal microscopy.

Effect of BCMs on the polarization of M-CSF-induced macrophages

The RAW264.7 cell line and GM-CSF-stimulated myeloid cells were chosen to evaluate the effect of BCMs on the polarization of macrophages. The cell culture procedure was performed as described in our previous report. Briefly, nontreated RAW264.7 cells were placed in a six-well plate with 1×105 cells in each well. After being cultured in an incubator with DMEM supplemented with 10% FBS for 8 h, LPS, IFN-γ, IL-4 and IL-10 were added to induce the polarization of the cells to the M1 or M_2 phenotype. After another 36 h, the medium was replaced with fresh medium, and BCMs at different final concentrations were added to the wells prepolarized with IL-4 and IL-10. Then, for flow cytometry, the cells were collected, stained with immunofluorescent antibodies, washed and measured by flow cytometry. For fluorescence imaging, at different time points, the cells were fixed with 4% paraformaldehyde for 20 min and then washed with PBS 3 times. The cells were permeabilized with 0.2% Triton X-100 for 5 min and then washed with PBS before blocking with BSA. For morphological observation, the cells were directly observed by optical microscopy after they were fixed with 4% paraformaldehyde for 20 min and washed with PBS 3 times.

After BMDMs were induced to differentiate into macrophages, BCMs were added to evaluate the effect of BCMs on the polarization of macrophages.

A similar procedure was used to evaluate the effect of BCMs on the polarization of M-CSF-induced BMDM-derived macrophages. After coincubation, the cells were collected and stained with aCD11b, aF4/80, aCD86, and aCD206. The proportions of different macrophage phenotypes were measured by flow cytometry.

In vitro *cytotoxicity of BCs, BMs and BCMs*

Several cell lines, including MC38 cancer cells, Jurkat cells, BMDM-derived DCs, BMDM-derived macrophages, and splenic T cells, were used to evaluate the cytotoxicity of BCMs. For MC38 cancer cells, Jurkat cells, BMDM-derived DCs, and BMDM-derived macrophages, CCK8 assays and apoptosis assays were performed according to standard procedures. In brief, the cells were placed on plates and cultured for 24 h, after which different formulations at different concentrations were added for further coculturing. At different time points, the cells were washed and stained according to the instructions of the CCK8 kit and Annexin V-EGFP apoptosis detection kit, respectively. The apoptosis of different cells was detected by flow cytometry.

In the case of splenic T cells, splenic T cells were extracted from the spleens of normal C57BL/6J mice. After being washed and treated with red blood cell lysis solution and further washed, the obtained splenic cells were cocultured with aCD3/aCD28 (1 μg/mL) for 48 h. Then, the cells were collected, washed and placed into a plate. Different BCMs at different concentrations were added to the plates for coculture with the induced T cells. After being cocultured for different durations, the cells were collected and stained with aCD45/aCD3/aCD4/aCD8/aPD-1/aTIM-3 according to the instructions of the Annexin V-EGFP apoptosis detection kit. The populations and apoptosis of different T cells were measured by flow cytometry.

In vivo tumor growth inhibition of BCs and BCMs in combination with a STING agonist and ICIs

An MC38 tumor model was established by subcutaneously injecting 5 × 105 MC38 cells or CT26 cells into the flanks of C57/B6J mice or BALB/c mice. When the tumor volume reached 50–100 mm^3, the mice were divided into different groups and subjected to different treatments.

To evaluate the effect of diAMP-BCMs on the lymphocytic microenvironment, MC38 tumor-bearing mice were divided into four groups and treated with saline, diAMP-BM, diAMP-BC, or diAMP-BCM. The formulations were intratumorally injected 3 times (once every 3 days). Three days after the final injection, the mice were sacrificed by anesthesia, and the tumors were eviscerated, digested and sieved for staining. The populations of T cells, monocytes, macrophages, DCs, etc., were measured by flow cytometry after staining for specific cell markers.

In the assay evaluating the dynamic variation in T cells in tumors after diAMP-BCM treatment, the mice were divided into 7 groups and treated with saline, BM, BC, BCM, or diAMP-BCM (three groups) by intratumoral injection. The mice in the four groups (treated with saline, BM, BC, BCM, or diAMP-BCM) were sacrificed by anesthesia on day 3 after the final injection, and the tumors were eviscerated, digested and sieved for staining. The remaining two groups treated with diAMP-BCM were sacrificed by anesthesia on day 1 and day 7 after the final injection, and the tumors were also eviscerated, digested and sieved for staining. The populations of T cells, NK cells, etc., were measured by flow cytometry after staining for specific cell markers.

In the assays evaluating the effect of the Cu/Mn ratio on tumor growth inhibition in vivo combined with aPD-1, the MC38-bearing mice were divided into 6 groups and treated with saline, diAMP-BM+aPD-1, diAMP-BC+aPD-1, diAMP-BCM+aPD-1 (Cu/Mn = 4:1), diAMP-BCM+aPD-1 (Cu/Mn = 1:1), or diAMP-BCM+aPD-1 (Cu/Mn = 0.25:1). diAMP-BM, diAMP-BC, or diAMP-BCM was intratumorally injected 3 times (once every 3 days), while aPD-1 was i.p. injected 5 times (once every other day, starting on day 1 after the first intratumoral injection).

In the assay evaluating the effect of diAMP-BCM+aPD-1 treatment on distal tumor growth inhibition, MC38 cells were subcutaneously injected into both flanks of C57/B6J mice, and when the tumor volume reached 50–100 mm^3, the mice were divided into four groups and treated with saline, diAMP+aPD-1, or diAMP-BCM+aPD-1 (Cu/Mn = 4:1). BC/BM represents the mixture of BC and BM. DiAMP and diAMP-BCM were intratumorally injected 3 times (once every 3 days), while aPD-1 was i.p. injected 5 times (once every other day, starting on day 1 after the first intratumoral injection). Three days after the final injection of aPD-1, the mice were sacrificed by anesthesia, and the tumors were removed, digested and sieved for staining. The populations of different types of T cells were measured by flow cytometry after staining for specific markers.

Transcriptome sequencing of tumor tissues or reprogrammed cells after different treatments

The transcriptional landscape of the tumors after different treatments was measured by transcriptome sequencing. After removal, the tumor tissues were precooled in liquid nitrogen and then stored at −80 °C before RNA extraction and purification. Total RNA was extracted from the tumor tissues before mRNA accumulation and purification. Then, fragmentation was performed to treat

the mRNA, and a sequencing library (with a paired-end library) was subsequently constructed. After quality evaluation, the samples were sequenced on an Illumina HiSeq platform. The sequencing data were analyzed on the GeneCloud platform.

In vivo tumor growth inhibition of aPD-1

MC38 cells (5×105) were subcutaneously implanted into the flanks of C57BL/6J mice (8 weeks old). When the average tumor volume reached 50–100 mm^3, the tumor-bearing mice were divided into two groups and treated with saline or aPD-1. aPD-1 was i.p. administered once every two days 5 times. The tumor volumes were recorded and calculated. On day 3 after the final administration, the mice were sacrificed under anesthesia, and the tumors were removed, digested and filtered for lymphocyte analysis. A similar procedure was used to measure lymphocytes in the spleen. aCD3, aCD3, aCD3, aPD-1, and aTIM-3 were used to identify lymphocyte populations by flow cytometry.

Multiplex immunohistochemical (mIHC) assays

mIHC assays were performed to evaluate the frequency of lymphocytes in the tumors after different treatments. The obtained tumor tissues were subjected to fluorescence staining with multiple antibodies, including aCD3 (CST78588), aCD8 (ABCAM217344), aPD-1 (CST84651), aTIM-3 (ABCAM241332), and aTCF-1 (CST2203). Semiquantitative analysis of the frequency and proportion of different lymphocytes was performed with the assistance of an absin. Ltd.

Statistical analysis and software

Statistical analysis was performed using SPSS 15.0 software (IBM Corporation, Armonk, NY, USA). The results are presented as the means ± SDs. Analysis of variance (ANOVA) was used for multiple group comparisons, and $p < 0.05$ was considered to indicate statistical significance.

Supplementary Information

The online version contains supplementary material available at https://doi.org/10.1186/s12951-024-02970-y.

Supplementary Material 1.

Acknowledgements

No applicable.

Author contributions

J. P., Q. Y. and Z. Q. conceived the project and were responsible for all phases of the research. J. P. and Q. Y. conceived and designed the experiment, and optimized the preparation of drug formulation. J. P. and Q. Y. participated in the design and supervision of in vitro and in vivo evaluation assays. R. L., Y. W., G. L. helped with operation and data analysis of cell culturing and flow cytometry. J. P. and Q. Y. analyzed the results of transcriptional sequence, therapeutic activities in vitro and in vivo. J. P., Q. Y., R. L. performed the literature review. J. P., Q. Y. and Z. Q. wrote the manuscript with the contributions of all authors. J. P., Q. Y. and Z. Q. provided conceptual advice and supervised the study. All authors have given approval to the final version of the manuscript.

Funding

This work was financially supported by the Key Research and Development Program of the Ministry of Science and Technology of Sichuan Province (2024YFFK0205 to J.R. Peng), and the Natural Science Foundation of Sichuan province (2024NSFSC0044 to Q. Yang), and the National Natural Science Foundation of China (NSFC 32171376 to J.R. Peng, 31930067 to Z.Y. Qian, 31871008 to J.R. Peng, 32371455 to Q. Yang); the Science and Technology Program for Distinguished Young Scholar of Sichuan Province (2020JDJQ0048 to Q. Yang); the Post-Doctor Research Project, West China Hospital, Sichuan University (Grant No. 18HXBH038 to J. R. Peng).

Availability of data and materials

No datasets were generated or analysed during the current study.

Declarations

Ethics approval and consent to participate

All animal procedures were performed following protocols approved by the Institutional Animal Care and Treatment Committee of Sichuan University (Chengdu, P. R. China) and West China Hospital, Sichuan University (Approved number: 2021755A) as well as Chengdu Medical College (Approved number: 2022037).

Consent for publication

Consents for publication were obtained from all the authors of this study.

Competing interests

The authors declare no competing interests.

Author details

[1]Department of Biotherapy, Cancer Center and State Key Laboratory of Biotherapy, West China Hospital, Sichuan University, Chengdu 610041, China. [2]Center of Scientific Research, Chengdu Medical College, Chengdu 610500, Sichuan, China.

Received: 5 July 2024 Accepted: 3 November 2024
Published online: 12 November 2024

References

1. Siegel RL, Wagle NS, Cercek A, Smith RA, Jemal A. Colorectal cancer statistics, 2023. CA Cancer J Clin. 2023;73(3):233–54.
2. Ganesh K, Stadler ZK, Cercek A, Mendelsohn RB, Shia J, Segal NH, Diaz LA Jr. Immunotherapy in colorectal cancer: rationale, challenges, and potential. Nat Rev Gastroenterol Hepatol. 2019;16(6):361–75.
3. Le DT, Uram JN, Wang H, et al. PD-1 blockade in tumors with mismatch-repair deficiency. N Engl J Med. 2015;372:2509–20.
4. Schmitt M, Greten FR. The inflammatory pathogenesis of colorectal cancer. Nat Rev Immunol. 2021;21:653–67.
5. André T, Shiu K-K, Kim TW, Jensen BV, Jensen LH, Punt C, Smith D, Garcia-Carbonero R, Benavides M, Gibbs P, de la Fouchardiere C, Rivera F, Elez E, Bendell J, Le DT, Yoshino T, Van Cutsem E, Yang P, Farooqui MZH, Marinello P, Diaz LA Jr, for the KEYNOTE-177 Investigators. Pembrolizumab in microsatellite-instability-high advanced colorectal cancer. N Engl J Med. 2020;383(23):2207–18.
6. Galon J, Bruni D. Approaches to treat immune hot, altered and cold tumours with combination immunotherapies. Nat Rev Drug Discov. 2019;18:197–218.
7. Cheng E, Shi Q, Shields AF, Nixon AB, Shergill AP, Ma C, Guthrie KA, Couture F, Kuebler P, Kumar P, Tan B, Krishnamurthi SS, Ng K, O'Reilly EM, Brown JC, Philip PA, Caan BJ, Cespedes Feliciano EM, Meyerhardt JA. Association of inflammatory biomarkers with survival among patients with stage III colon cancer. JAMA Oncol. 2023;9(3):404–13.
8. Sui Q, Zhang Xi, Chen C, Tang J, Jiehai Yu, Li W, Kai Han Wu, Jiang LL, Kong L, Li Y, Hou Z, Zhou C, Zhang C, Zhang L, Xiao B, Mei W, Yanbo Xu, Qin J,

Zheng J, Pan Z, Ding P-R. Inflammation promotes resistance to immune checkpoint inhibitors in high microsatellite instability colorectal cancer. Nat Commun. 2022;13:7316.
9. Propper DJ, Balkwill FR. Harnessing cytokines and chemokines for cancer therapy. Nat Rev Clin Oncol. 2022;19:237–53.
10. Tjader NP, Toland AE. Immunotherapy for colorectal cancer: insight from inherited genetics. Trends Cancer. 2024;10(5):444–56.
11. Ben-Neriah Y, Karin M. Inflammation meets cancer, with NF-Kb as the matchmaker. Nat Immunol. 2011;12:715–23.
12. Guo Q, Jin Y, Chen X, Ye X, Shen X, Lin M, Zeng C, Zhou T, Zhang J. NF-kB in biology and targeted therapy: new insights and translational implications. Signal Transduct Target Ther. 2024;9:53.
13. Demaria O, Cornen S, Daëron M, Morel Y, Medzhitov R, Vivier E. Harnessing innate immunity in cancer therapy. Nature. 2019;574:45–56.
14. Kirchhammer N, Trefny MP, Auf der Maur P, Läubli H, Zippelius A. Combination cancer immunotherapies: emerging treatment strategies adapted to the tumor microenvironment. Sci Transl Med. 2022;14: eabo3605.
15. Yan Yu, Pan M, Peng J, Danrong Hu, Hao Y, Qian Z. A review on recent advances in hydrogen peroxide electrochemical sensors for application in cell detection. Chin Chem Lett. 2022;33(9):4133–45.
16. Xin Yu, Wang Y, Zhang J, Liu J, Wang A, Ding L. Recent development of copper-based nanozymes for biomedical applications. Adv Healthc Mater. 2024;13:2302023.
17. Li Z, Xie CJ, Ren XW, Zhang Q, Ma BJ. CuS nanoenzyme against bacterial infection by in situ hydroxyl radical generation on bacteria surface. Rare Met. 2023;6:1899–911.
18. Chang M, Hou Z, Wang M, Wen D, Li C, Liu Y, Zhao Y, Lin J. Cu single atom nanozyme based high-efficiency mild photothermal therapy through cellular metabolic regulation. Angew Chem Int Ed. 2022;61: e202209245.
19. Li Y, Dong Ya, Zhou X, Fan K. Nanotechnology connecting copper metabolism and tumor therapy. MedComm-Biomater Appl. 2023;2(2): e36.
20. Liu T, Xiao B, Xiang F, Tan J, Chen Z, Zhang X, Chengzhou Wu, Mao Z, Luo G, Chen X, Deng J. Ultrasmall copper-based nanoparticles for reactive oxygen species scavenging and alleviating of inflammation related disease. Nat Commun. 2020;11:2788.
21. Peng J, Dong M, Ran B, Li W, Hao Y, Yang Q, Tan L, Shi K, Qian Z. "One-for-all"-type, biodegradable prussian blue/manganese dioxide hybrid nanocrystal for trimodal imaging-guided photothermal therapy and oxygen regulation of breast cancer. ACS Appl Mater Interfaces. 2017;9:13875–86.
22. Lin L-S, Song J, Song L, Ke K, Liu Y, Zhou Z, Shen Z, Li J, Yang Z, Tang W, Niu G, Yang H-H, Chen X. Simultaneous Fenton-like ion delivery and glutathione depletion by MnO_2-based nanoagent to enhance chemodynamic therapy. Angew Chem Int Ed. 2018;57:4902–6.
23. Wang C, Guan Y, Lv M, Zhang R, Guo Z, Wei X, Xiaoxia Du, Yang J, Li T, Wan Yi, Xiaodong Su, Huang X, Jiang Z. Manganese increases the sensitivity of the cGAS-STING pathway for double-stranded DNA and is required for the host defense against DNA viruses. Immunity. 2018;48:675–87.
24. Li X, Liu H, Gao W, Yang Q, Li X, Zhou X, Wang L, Lu Z, Liu J, Luo A, Chen C, Liu Z, Zhao Y. Octadecyl gallate and lipid-modified $MnSe_2$ nanoparticles enhance radiosensitivity in esophageal squamous cell carcinoma and promote radioprotection in normal tissues. Adv Mater. 2024;36:2311291. https://doi.org/10.1002/adma.202311291.
25. Wang Y, Li S, Hu M, Yang Y, McCabe E, Zhang L, Withrow AM, Ting JP, Liu R. Universal STING mimic boosts antitumour immunity via preferential activation of tumour control signaling pathways. Nat Nanotechnol. 2024. https://doi.org/10.1038/s41565-024-01624-2.
26. Li J, Hubisz MJ, Earlie EM, Duran MA, Hong C, Varela AA, Lettera E, Deyell M, Tavora B, Havel JJ, Phyu SM, Amin AD, Budre K, Kamiya E, Cavallo J-A, Garris C, Powell S, Reis-Filho JS, Wen H, Bettigole S, Khan AJ, Izar B, Parkes EE, Laughney AM, Bakhoum SF. Non-cell-autonomous cancer progression from chromosomal instability. Nature. 2023;620:1–9. https://doi.org/10.1038/s41586-023-06464-z.
27. Liang J-L, Jin X-K, Zhang S-M, Huang Q-X, Ji P, Deng X-C, Cheng S-X, Chen W-H, Zhang X-Z. Specific activation of cGAS-STING pathway by nanotherapeutics-mediated ferroptosis evoked endogenous signaling for boosting systemic tumor immunotherapy. Sci Bull. 2023;68:622–36.
28. Sun X, Zhang Y, Li J, Park KS, Han K, Zhou X, Xu Y, Nam J, Xu J, Shi X, Mei L, Lei YL, Moon JJ. Amplifying STING activation by cyclic dinucleotide-manganese particles for local and systemic cancer metalloimmunotherapy. Nat Nanotechnol. 2021;16:1260–70.
29. Wang C, Sharma N, Kessler PM, Sen GC. Interferon induction by STING requires its translocation to the late endosomes. Traffic. 2023;24:576–86.
30. Luo Y, Chang L, Ji Y, Liang T. ER: a critical hub for STING signaling regulation. Trends Cell Biol. 2024. https://doi.org/10.1016/j.tcb.2024.02.006.
31. Zhang B-C, Nandakumar R, Reinert LS, et al. STEEP mediates STING ER exit and activation of signaling. Nat Immunol. 2020;21:868–79.
32. Yuan X, Yin Y, Zan W, Sun X, Yang Q. Hybrid manganese dioxide-bovine serum albumin nanostructure incorporated with doxorubicin and IR780 for enhanced breast cancer chemo-photothermal therapy. Drug Deliv. 2019;26:1254–64.
33. Xiao Y, Peng J, Liu Q, Chen L, Shi K, Han R, Yang Q, Zhong L, Zha R, Qu Y, Qian Z. Ultrasmall CuS@BSA nanoparticles with mild photothermal conversion synergistically induce MSCs-differentiated fibroblast and improve skin regeneration. Theranostics. 2020;10(4):1500–13.
34. Xia H, Green DR, Zou W. Autophagy in tumour immunity and therapy. Nat Rev Cancer. 2021;21:281–97.
35. Ganesh K, Stadler ZK, Cercek A, Mendelsohn RB, Shia J, Segal NH, Diaz LA Jr. Immunotherapy in colorectal cancer: rationale, challenges and potential. Nat Rev Gastroenterol Hepatol. 2019;16:361–75.
36. Li J, Cheng Wu, Huabin Hu, Qin Ge, Xueqian Wu, Bai F, Zhang J, Cai Y, Huang Y, Wang C, Yang J, Luan Y, Jiang Z, Ling J, Zehua Wu, Chen Y, Xie Z, Deng Y. Remodeling of the immune and stroma cell compartment by PD-1 blockade in mismatch repair-deficient colorectal cancer. Cancer Cell. 2023;41:1152–69.
37. Peng J, Yang Q, Jiang H, Wang Y, Liu Q, Xiao Y, Qian Z. Amplifying cancer chemoimmunotherapy though F4/80+CD11c+ DC-like macrophages induced by micellar docetaxel together with a TLR7/8 nanoagonist. Nano Today. 2024;54: 102087.
38. Kersten K, Hu KH, Combes AJ, Samad B, Harwin T, Ray A, Rao AA, Cai E, Marchuk K, Artichoker J. Spatiotemporal co-dependency between macrophages and exhausted CD8+ T cells in cancer. Cancer Cell. 2022;40:624-638.e629.
39. Congy-Jolivet N, Cenac C, Dellacasagrande J, Puissant-Lubrano B, Apoil PA, Guedj K, Abbas F, Laffont S, Sourdet S, Guyonnet S, Nourhashemi F, Guery J-C, Blancher A. Monocytes are the main source of STING-mediated IFN-alpha production. EBioMedicine. 2022;80: 104047.
40. Vanhersecke L, Brunet M, Guegan J-P, et al. Mature tertiary lymphoid structures predict immune checkpoint inhibitor efficacy in solid tumors independently of PD-L1 expression. Nat Cancer. 2021;2:794–802.
41. Cabrita R, Lauss M, Sanna A, et al. Tertiary lymphoid structures improve immunotherapy and survival in melanoma. Nature. 2020;577:561–5.
42. Dieu-Nosjean MC, Goc J, Giraldo NA, Sautès-Fridman C, Fridman WH. Tertiary lymphoid structures in cancer and beyond. Trends Immunol. 2014;35(11):571–80.
43. Peng J, Yang Q, Shi K, Xiao Y, Wei X, Qian Z. Intratumoral fate of functional nanoparticles in response to microenvironment factor: implications on cancer diagnosis and therapy. Adv Drug Deliv Rev. 2019;143:37–67.
44. Agarwal D, Goodison S, Nicholson B, Tarin D, Urquidi V. Expression of matrix metalloproteinase 8 (MMP-8) and tyrosinase-related protein-1 (TYRP-1) correlates with the absence of metastasis in an isogenic human breast cancer model. Differentiation. 2003;71:114–25.
45. McCawley LJ, Crawford HC, King LE, Mudgett J, Matrisian LM. A protective role for matrix metalloproteinase-3 in squamous cell carcinoma. Can Res. 2004;64:6965–72.
46. Mlecnik B, Bindea G, Kirilovsky A, Angell HK, Obenauf AC, Tosolini M, Church SE, Maby P, Vasaturo A, Angelova M, Fredriksen T, Mauger S, Waldner M, Berger A, Speicher MR, Pagès F, Valge-Archer V, Galon J. The tumor microenvironment and Immunoscore are critical determinants of dissemination to distant metastasis. Sci Transl Med. 2016;8:327ra26.
47. Mlecnik B, Bindea G, Angell HK, Maby P, Angelova M, Tougeron D, Church SE, Lafontaine L, Fischer M, Fredriksen T, Sasso M, Bilocq AM, Kirilovsky A, Obenauf AC, Hamieh M, Berger A, Bruneval P, Tuech J-J, Sabourin J-C, Le Pessot F, Mauillon J, Rafii A, Laurent-Puig P, Speicher MR, Trajanoski Z, Michel P, Sesboue R, Frebourg T, Pagès F, Valge-Archer V, Latouche J-B, Galon J. Integrative analyses of colorectal cancer show Immunoscore is a stronger predictor of patient survival than microsatellite instability. Immunity. 2016;44:698–711.
48. Pauken KE, Sammons MA, Odorizzi PM, Manne S, Godec J, Khan O, Drake AM, Chen Z, Sen DR, Kurachi M, Barnitz RA, Bartman C, Bengsch B, Huang

AC, Schenkel JM, Vahedi G, Haining WN, Berger SL, Wherry EJ. Epigenetic stability of exhausted T cells limits durability of reinvigoration by PD-1 blockage. Science. 2016;354:1160–5.
49. Bell HN, Huber AK, Singhal R, Korimerla N, Rebernick RJ, Kumar R, Elderany MO, Sajjakulnukit P, Das NK, Kerk SA, Solanki S, James JG, Kim D, Zhang L, Chen B, Mehra R, Frankel TL, Gyorffy B, Fearon ER, di Magliano MP, Gonzalez FJ, Banerjee R, Wahl DR, Lyssiotis CA, Green M, Shah YM. Microenvironmental ammonia enhances T cell exhaustion in colorectal cancer. Cell Metab. 2023;35:134–49.
50. Rudloff MW, Zumbo P, Favret NR, Roetman JJ, Detrés Román CR, Erwin MM, Murray KA, Jonnakuti ST, Dündar F, Betel D, Philip M. Hallmarks of CD8+ T cell dysfunction are established within hours of tumor antigen encounter before cell division. Nat Immunol. 2023. https://doi.org/10.1038/s41590-023-01578-y.
51. Daniel B, Yost KE, Hsiung S, Sandor K, Xia Y, Qi Y, Hiam-Galvez KJ, Black M, Raposo CJ, Shi Q, Meier SL, Belk JA, Giles JR, Wherry EJ, Chang HY, Egawa T, Satpathy AT. Divergent clonal differentiation trajectories of T cell exhaustion. Nat Immunol. 2022;23:1614–27.
52. Philip M, Schietinger A. CD8+ T cell differentiation and dysfunction in cancer. Nat Rev Immunol. 2022;22:209–23.
53. Prasad R, Jyothi VG, Kommineni N, Bulusu RT, Mendes BB, Lovell JF, Conde J. Biomimetic ghost nanomedicine-based optotheranostics for cancer. Nano Lett. 2024;24:8217–31.
54. Prasad R, Peng B, Mendes BB, Kilian HI, Gorain M, Zhang H, Kundu GC, Xia J, Lovell JF, Conde J. Biomimetic bright optotheranostics for metastasis monitoring and multimodal image-guided breast cancer therapeutics. J Control Release. 2024;367:300–15.
55. Prasad R, Kumari R, Chaudhari R, Kumar R, Kundu GC, Kumari S, Roy G, Gorain M, Chandra P. Emissive lipid nanoparticles as biophotonic contrast agent for site-selective solid tumor imaging in pre-clinical models. ACS Appl Mater Interfaces. 2024;16(40):53393–404.

Publisher's Note